

REPORT DOCUMENTATION PAGE				Form Approved OMB No. 0704-0188	
Public reporting burden for this collection of information is estimated to average 1 hour per response, including the time for reviewing instructions, searching existing data sources, gathering and maintaining the data needed, and completing and reviewing the collection of information. Send comments regarding this burden estimate or any other aspect of this collection of information, including suggestions for reducing the burden, to Department of Defense, Washington Headquarters Services, Directorate for Information Operations and Reports (0704-0188), 1215 Jefferson Davis Highway, Suite 1204, Arlington, VA 22202-4302. Respondents should be aware that notwithstanding any other provision of law, no person shall be subject to any penalty for failing to comply with a collection of information if it does not display a currently valid OMB control number. <b>PLEASE DO NOT RETURN YOUR FORM TO THE ABOVE ADDRESS.</b>					
<b>1. REPORT DATE (DD-MM-YYYY)</b>		<b>2. REPORT TYPE</b> Final Report		<b>3. DATES COVERED (From - To)</b> 01-Nov-03 - 01-Nov-04	
<b>4. TITLE AND SUBTITLE</b> Hybrid Antenna Amplifier: A Controllable High Power Microwave Source				<b>5a. CONTRACT NUMBER</b> ISTC Registration No: 2823	
				<b>5b. GRANT NUMBER</b>	
				<b>5c. PROGRAM ELEMENT NUMBER</b>	
				<b>5d. PROJECT NUMBER</b>	
<b>6. AUTHOR(S)</b> Dr. Anatoli Shlapakovski				<b>5d. TASK NUMBER</b>	
				<b>5e. WORK UNIT NUMBER</b>	
<b>7. PERFORMING ORGANIZATION NAME(S) AND ADDRESS(ES)</b> Nuclear Physics Institute at Tomsk Polytechnic University P.O. Box 25 Tomsk 634050 Russia				<b>8. PERFORMING ORGANIZATION REPORT NUMBER</b>  N/A	
<b>9. SPONSORING/MONITORING AGENCY NAME(S) AND ADDRESS(ES)</b> EOARD PSC 802 BOX 14 FPO 09499-0014				<b>10. SPONSOR/MONITOR'S ACRONYM(S)</b>	
				<b>11. SPONSOR/MONITOR'S REPORT NUMBER(S)</b> ISTC 01-7045	
<b>12. DISTRIBUTION/AVAILABILITY STATEMENT</b> Approved for public release; distribution is unlimited.					
<b>13. SUPPLEMENTARY NOTES</b>					
<b>14. ABSTRACT</b>  This report results from a contract tasking Nuclear Physics Institute at Tomsk Polytechnic University as follows: The contractor will evaluate the concept of hybrid antenna-amplifiers, i.e., devices representing a combination of a surface wave antenna and a traveling wave tube. Theoretical investigations and numerical simulations (including particle-in-cell simulations and complex calculations using existing electromagnetic codes) as well as prototype experiments on electron beam transport (in the absence of the antenna feed signal) and microwave transmission (in the absence of the electron beam) are planned.					
<b>15. SUBJECT TERMS</b> EOARD, Physics, Electricity and Magnetism					
<b>16. SECURITY CLASSIFICATION OF:</b>			<b>17. LIMITATION OF ABSTRACT</b> UL	<b>18. NUMBER OF PAGES</b>  46	<b>19a. NAME OF RESPONSIBLE PERSON</b> MICHAEL KJ MILLIGAN, Lt Col, USAF
<b>a. REPORT</b> UNCLAS	<b>b. ABSTRACT</b> UNCLAS	<b>c. THIS PAGE</b> UNCLAS			<b>19b. TELEPHONE NUMBER (Include area code)</b> +44 (0)20 7514 4955

**ISTC 2823p**

**Final  
Project Technical Report  
of ISTC 2823p**

**Hybrid Antenna Amplifier: a Controllable High Power  
Microwave Source**

**(From 1 November 2003 to 31 October 2004 for 12 months)**

**Anatoli Solomonovich Shlapakovski  
(Project Manager)  
Nuclear Physics Institute at Tomsk Polytechnic University**

**March 2005**

**20060414056**

**ISTC-01-7045  
DTIC Copy  
Distribution A:  
Approved for public release;  
distribution is unlimited.**

---

**This work was supported financially by EOARD and performed under the contract to the International Science and Technology Center (ISTC), Moscow.**

## LIST OF CONTENTS

I. Introduction	3
II. Tasks and results obtained	5
1. Task 1. Theoretical exploration of the concept of antenna-amplifiers	5
a) 1-D multimode simulations	5
b) 3-D particle-in-cell simulations	12
c) Linear theory for conducting, disc-loaded rod	21
2. Task 2. Experimental exploration of the concept of antenna-amplifiers	25
a) LIA module design	25
b) Annular beam generation and transport with a dielectric inside	29
c) Microwave transmission and antenna pattern measurements	37
III. Conclusions	42
IV. References	44
V. Presentation of results	45

## I. INTRODUCTION

Electron beam interaction with electromagnetic waves whose phase velocities are slowed down to be in synchronism with the electron velocities is the physical basis of operation of traveling wave tubes and backward wave oscillators, coherent microwave radiation sources allowing control of radiation characteristics. With high-current relativistic electron beams delivered from high-current pulsed power accelerators, one can generate and amplify high-power microwaves achieving  $10^7$  to  $10^{10}$  W output power levels at  $10^{-9}$  to  $10^{-6}$  s pulse durations. There has been much progress in this field since the beginning of the 1970's [1] and in the last decade [2]. The development of relativistic backward wave oscillators has resulted in its application as a radar transmitter unit [3]. More opportunities for control of radiation parameters are offered by amplifiers (wider power range and frequency bandwidth, possibility of a phase control), so that relativistic traveling wave tubes (TWT), wide-bandwidth dielectric and plasma Cherenkov maser amplifiers [4-6] are developed as well. In all these configurations, a relativistic electron beam propagates within some slow wave supporting structure.

Meanwhile, the conditions of synchronous Cherenkov beam-wave interaction are also appropriate for surface wave antennas. For instance, for the well-developed dielectric rod antenna [7], the operating mode has a subluminal phase velocity and axial electric field component outside a rod. Hence, if an annular relativistic beam propagates along the rod surface, it can amplify an antenna feed signal, *i.e.*, the antenna feed signal would simultaneously serve as the TWT RF drive. This means that there is neither need for a transmission line between the amplifier and antenna, nor for a mode converter providing appropriate field structure to antenna feeding. Such a hybrid configuration that was called an antenna-amplifier [8] would yield a compact source of high-power microwaves with the added benefit of controllable power, frequency spectrum, phase, and also extracted microwave beam. The device may have wide bandwidth and high directivity. This could significantly extend the area of application of high power microwave sources, in particular, to applications in surveillance and electronics countermeasure systems.

The antenna-amplifier concept can be realized when an electron beam is generated by a module of a linear induction accelerator (LIA) as shown in Fig.1. Due to the physical principles of LIA operation (the electric field is induced by magnetic flux variation in the toroidal inductors), the cathode holder from the external side is at ground potential. Hence, it can be connected to an external microwave source, and the hollow cathode holder serves as the antenna feed waveguide. Linear induction accelerators are compact and capable of high repetition rate operation, a trait that is important for practical applications.

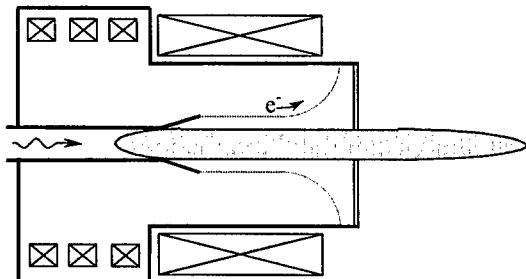


Fig.1. Hybrid antenna-amplifier (schematic). The feed waveguide of the rod antenna is the cathode holder of LIA module. It is at ground potential. The generated electron beam amplifies the feed signal due to the TWT interaction mechanism.

There is a significant physical peculiarity of the system shown in Fig.1. The operating mode of a rod antenna is the fundamental non-axisymmetric  $HE_{11}$  mode that is atypical for conventional TWTs, which operate in symmetric TM modes. In the work [8], a linear theory was developed for the annular beam instability in a circular waveguide with an inner dielectric rod for the general, non-axisymmetric case. It was found that, depending on the geometry, the  $HE_{11}$  mode can be the dominant mode, or there can be no prevalence of this mode in the instability spectrum. This was the first step in the

exploration of the antenna-amplifier concept. Later, the nonlinear theory was formulated accounting for asymmetry of RF fields and possibility of beam interaction with higher-order modes at harmonics of the drive signal frequency [9], and initial 3-D numerical simulations were carried out [10].

In this project, a further development of the described idea has been accomplished. The objectives of this project were to explore the concept of hybrid antenna-amplifier in much more details through theoretical investigations, numerical simulations, and experiments and to elaborate an initial design of the antenna-amplifier device that is based on a dielectric rod antenna and driven by an electron beam produced in a compact LIA module.

The scope of project activities included two tasks. The first task was the theoretical exploration of the concept of antenna-amplifiers. It was necessary to investigate specific nonlinear effects in TWT interaction caused by the azimuthal dependence of microwave drive field, i.e., harmonic generation due to electron beam interaction with higher-order modes of the system. The approach for that was in performing 1-D multimode simulations based on the developed multimode nonlinear theory accounting for an arbitrary number of modes potentially synchronous to the beam at some harmonic of the drive frequency. Also planned were particle-in-cell simulations using the 3-D version of the code MAGIC applicable to the case of non-axisymmetric operating mode. Full-scale numerical experiments taking into account the peculiarities of geometry, effects of electron beam explosive emission model, and particles transverse motion had to verify the results of the simplified 1-D theory and fix the initial design of the hybrid antenna-amplifier. Additional particular problem in the scope of theoretical exploration was the development of linear theory for the case of disc-loaded conducting rod in order to make a comparison with the device based on a dielectric rod antenna. This had to make clear whether conducting surface wave antenna could be preferable for the antenna-amplifier device to be based on, since in the absence of dielectric, there are no problems connected with the near-surface plasma formation.

The second task was the experimental exploration of the concept of antenna-amplifiers. It assumed, before all, the modification of the LIA module and fabrication of the hardware necessary to conduct the model experiments planned. The key model experiments connected with the problem mentioned above were the experiments on the LIA module on annular electron beam generation and transportation with a dielectric rod inside. They were supposed to clarify whether plasma formation takes place at the dielectric surface in the device without a microwave drive signal and to estimate a density of this plasma in order to conclude how strongly it can affect microwave transmission. The approach for that was in implementing diagnostics using electron saturation current measurements. Another part of the experimental program was in studying microwave transmission through the system and radiated antenna pattern in the absence of electron beam. These experiments were supposed to make clear how the actual geometry of the device affects the antenna efficiency. Standard methods of microwave antenna measurements were employed, with the use of low power X-band frequency tunable generator, to determine the level of reflections and angular dependences of radiation power in the far field region.

It should be acknowledged here that the possibility to use the code MAGIC for particle-in-cell simulations was kindly given to the project manager at the University of New Mexico, USA and Nagaoka University of Technology, Japan due to invaluable cooperation of Prof. Edl Schamiloglu (UNM) and Dr. Weihua Jiang (NUT).

## II. TASKS AND RESULTS OBTAINED

### 1. Task 1. Theoretical exploration of the concept of antenna-amplifiers

#### a) 1-D multimode simulations

For the antenna-amplifier device, the process of electron beam interaction with a synchronous electromagnetic wave at the nonlinear stage may significantly differ from that occurring in conventional TWTs because of the specific character of its operating mode, non-axisymmetric  $HE_{11}$  mode. Differences concern the effect of the drive frequency harmonics generation, which is known for TWTs with bandwidth greater than an octave bandwidth [11]. For the antenna-amplifier, it was seen from the results of the spatial growth rate calculations [8] that multiples of the fundamental  $HE_{11}$  mode amplification band frequencies might reside within the amplification bands of the higher-order modes. If a microwave drive signal enters the interaction space in a symmetric TM mode (that is usual for classical TWTs), no asymmetric modes can be excited because of the orthogonality of the eigenfunctions for RF fields with respect to the symmetric ac current. The opposite is not the case with the asymmetric  $HE_{11}$  mode, which can induce, due to nonlinearity, any azimuthal harmonic of ac current in the large signal regime. Therefore, for the antenna-amplifier, the spectrum of modes that are able to couple to the beam is not limited by the set of modes with a common azimuthal index, and harmonics of the drive frequency are generated in higher-order modes.

In addition, coupling of higher-order modes to the beam at harmonic frequencies can be significant since for the  $HE_{11}$  mode, the microwave power is distributed over the whole dielectric rod transverse cross-section, whereas for other modes, it is concentrated near the rod surface. Thus, the same power corresponds to larger  $E_z$ -component at the beam radius for higher-order modes. This can lead to a power level of radiation at harmonic frequencies comparable to, and even exceeding that of the main signal, in difference of classical large bandwidth TWT amplifiers where harmonics power level is typically much less than that of the main signal. Hence, multimode simulations are needed for the antenna-amplifier to show the degree of harmonics growth at different parameters of the system.

The set of equations allowing for such simulations is similar to that from nonlinear TWT theory [12], but takes into account an arbitrary number of modes potentially synchronous to the beam at some harmonic of the main frequency. This means that for each particle, there must be a separate equation for its phase with respect to each mode  $\alpha$  involved into the interaction process  $\theta_\alpha = n_\alpha \omega t - k_{0\alpha} (n_\alpha \omega) z$ , where  $\omega$  is the drive frequency,  $n_\alpha$  is a harmonic number, and  $k_{0\alpha}$  is a mode axial wavenumber. With the assumption of zero beam thickness, this equation is written as follows:

$$\frac{d\theta_\alpha}{dz} = \frac{n_\alpha \omega}{u(z, \varphi, t_0)} - k_{0\alpha}.$$

Here  $u$  is a particle velocity,  $t_0$  is a moment of its entering into the interaction space, and  $\varphi$  is its azimuthal position. Particle motion and RF fields depend on  $\varphi$ . The equation of excitation [12] for a mode with azimuthal index  $l_\alpha$  can be presented in the following form:

$$\frac{dE_\alpha}{dz} = - \frac{\Phi_\alpha^2(r_b)}{4P_\alpha} \frac{I}{2\pi^2 n_\alpha} \int_0^{2\pi} d\varphi \int_0^{2\pi m_\alpha} e^{i[\theta_\alpha(z, \varphi, \theta_{0\alpha}) - l_\alpha \varphi]} d\theta_{0\alpha},$$

where  $E_\alpha$  stands for a mode complex amplitude at the beam radius  $r_b$ , the ratio of the square of the electric field  $z$ -component  $\Phi_\alpha$  to the power  $P_\alpha$  represents a mode coupling coefficient,  $I$  is the beam current, and  $\theta_{0\alpha} = n_\alpha \omega t_0$  is the initial phase of a particle with respect to the given

mode. The relativistic equation of motion in 1-D case and without taking into consideration non-synchronous ac space charge fields is:

$$\frac{du}{dz} = \frac{e}{mu} \left(1 - \frac{u^2}{c^2}\right)^{3/2} \sum_{\alpha} \operatorname{Re}\{E_{\alpha}(z) e^{-i[\theta_{\alpha}(z, \varphi, \theta_{0\alpha}) - l_{\alpha}\varphi]}\},$$

where  $e$ ,  $m$ ,  $c$  stand for the electron charge, rest mass, and the speed of light, respectively.

Introducing the suitable normalized variables

$$\zeta = C_1 \frac{\omega}{u_0} z, \quad v = \frac{v_0}{C_1}, \quad v_0 = 1 - \frac{u}{u_0}, \quad \tilde{E}_{\alpha} = -\frac{1}{C_1^2} \frac{eE_{\alpha}}{\gamma^3 m \omega u_0},$$

as well as the mismatch parameters and analogues of Pierce parameter for each mode

$$\delta_{\alpha} = \frac{1}{C_1} \left( \frac{k_{0\alpha} u_0}{n_{\alpha} \omega} - 1 \right), \quad C_{\alpha}^3 = \frac{eI}{\gamma^3 m \omega^2} \frac{\Phi_{\alpha}^2(r_b)}{4P_{\alpha}},$$

where  $u_0$  is the initial value of electrons velocity,  $\gamma$  is corresponding Lorentz factor,  $C_1^3$  is the Pierce parameter corresponding to the fundamental  $\text{HE}_{11}$  mode, and assuming that  $v_0 \ll 1$ , one can obtain the following set of equations used in our 1-D multimode simulations:

$$\begin{aligned} \frac{d\tilde{E}_{\alpha}}{d\zeta} &= \frac{1}{2\pi^2} \frac{C_{\alpha}^3}{n_{\alpha} C_1^3} \int_0^{2\pi} d\varphi \int_0^{2m_{\alpha}} e^{i(\theta_{\alpha} - l_{\alpha}\varphi)} d\theta_{0\alpha} \\ \frac{d\theta_{\alpha}}{d\zeta} &= n_{\alpha} (v - \delta_{\alpha}) \\ \frac{dv}{d\zeta} &= [1 + 2(\gamma^2 - 1)C_1 v]^{3/2} \sum_{\alpha} \operatorname{Re}\{\tilde{E}_{\alpha} e^{-i(\theta_{\alpha} - l_{\alpha}\varphi)}\} \end{aligned}$$

So, each mode involved into simulations is characterized with its own azimuthal index, harmonic number, mismatch parameter, and coupling (Pierce) parameter. It is also necessary to take into account the degeneracy of non-axisymmetric modes. This is accomplished by accounting for modes with both positive and negative values of the azimuthal index. As a result, one can perform simulations for arbitrary structure of the input signal field: fixed, azimuthally rotating, or some mixed, just setting proper initial conditions for the amplitudes of the modes.

Finally, the microwave power transmitted in the mode  $\alpha$  normalized to the kinetic beam power at the entrance is given by the expression:

$$\frac{P_{\alpha}}{P_{\text{beam}}} = \frac{\gamma(\gamma + 1)}{4} \frac{C_1^4}{C_{\alpha}^3} |\tilde{E}_{\alpha}|^2.$$

For non-axisymmetric modes, the power is a sum of contributions from positive and negative azimuthal index values.

The actual values of mismatch and Pierce parameters  $\delta_{\alpha}$  and  $C_{\alpha}^3$  for different modes required for simulations are calculated from the numerical solution of the dispersion relations (yielding  $k_{0\alpha}$ ) and integrating Poynting vector profiles over the cross-section of the circular waveguide with an inner dielectric rod (that yields  $P_{\alpha}$ ). Corresponding expressions are known (see, for instance, [13]). The dispersion relation can be written as (index  $\alpha$  is further omitted):

$$\left[ \frac{pF'_E(qa, qb)}{F_E(qa, qb)} + \varepsilon \frac{qj'_l(pa)}{j_l(pa)} \right] \left[ \frac{pF'_H(qa, qb)}{F_H(qa, qb)} + \frac{qj'_l(pa)}{j_l(pa)} \right] = \left[ (\varepsilon - 1)l \frac{n\omega}{c} \frac{k_0}{pqa} \right]^2.$$

Here,  $p^2 = \varepsilon \frac{(n\omega)^2}{c^2} - k_0^2$ ,  $q^2 = k_0^2 - \frac{(n\omega)^2}{c^2}$ ,  $\varepsilon$  is the dielectric constant,  $a$  is the rod radius,  $b$  is the waveguide radius,  $j_l$  is Bessel function of  $l$ th order, and other functions are:

$$\begin{aligned} F_E(x, y) &= I_l(x)K_l(y) - I_l(y)K_l(x), & F'_E(x, y) &= I'_l(x)K_l(y) - I_l(y)K'_l(x), \\ F_H(x, y) &= I_l(x)K'_l(y) - I'_l(y)K_l(x), & F'_H(x, y) &= I'_l(x)K'_l(y) - I'_l(y)K'_l(x), \end{aligned}$$

where  $I_l$  and  $K_l$  are modified Bessel functions.

The power is calculated through the transverse RF field components

$$P = \frac{c}{4} \int_0^b \text{Re}(E_r H_\phi^* - E_\phi H_r^*) r dr = \frac{c}{4} \int_0^b S_z(r) r dr,$$

where the function  $S_z$  giving the radial profile of Poynting vector axial component is expressed through the radial profiles of axial electric and magnetic fields ( $\Phi$  and  $\Psi$ ) as follows.

In dielectric region ( $r < a$ ),

$$S_z = \frac{1}{p^4} \left\{ \frac{k_0 n \omega}{c} \left[ \varepsilon \left( \frac{d\Phi}{dr} \right)^2 + \left( \frac{d\Psi}{dr} \right)^2 + \frac{l^2}{r^2} (\varepsilon \Phi^2 + \Psi^2) \right] - \frac{l}{r} \left( k_0^2 + \varepsilon \frac{(n\omega)^2}{c^2} \right) \frac{d(\Phi\Psi)}{dr} \right\}.$$

In vacuum region ( $a < r < b$ ),

$$S_z = \frac{1}{q^4} \left\{ \frac{k_0 n \omega}{c} \left[ \left( \frac{d\Phi}{dr} \right)^2 + \left( \frac{d\Psi}{dr} \right)^2 + \frac{l^2}{r^2} (\Phi^2 + \Psi^2) \right] - \frac{l}{r} \left( k_0^2 + \frac{(n\omega)^2}{c^2} \right) \frac{d(\Phi\Psi)}{dr} \right\}.$$

The profiles of axial fields here are following ( $E_0$  is an amplitude):

$$\Phi(r) = E_0 \begin{cases} j_l(pr), & r < a \\ j_l(pa) \frac{F_E(qr, qb)}{F_E(qa, qb)}, & a < r < b \end{cases} \quad \Psi(r) = E_0 G_l \begin{cases} j_l(pr), & r < a \\ j_l(pa) \frac{F_H(qr, qb)}{F_H(qa, qb)}, & a < r < b \end{cases}$$

where

$$G_l = \frac{(\varepsilon - 1) \frac{l}{a} k_0 \frac{n\omega}{c}}{qp \left[ \frac{pF'_H(qa, qb)}{F_H(qa, qb)} + \frac{qj'_l(pa)}{j_l(pa)} \right]}.$$

In all simulations performed, the particle ensemble was uniformly distributed over the intervals  $(0, 2\pi)$  in azimuthal positions and initial phases with respect to the  $\text{HE}_{11}$  mode (for multiple frequencies, initial phases are distributed respectively between 0 and  $2\pi n_a$ ). Typically,  $48 \times 48$  particles were utilized. There was also no velocity modulation set at the entrance ( $v = 0$  for all particles). Most of the simulations were performed accounting for the five modes, the  $\text{HE}_{11}$  mode at the main frequency and the four higher-order modes, which, as was seen from spatial growth rate calculations [8], might be excited at its multiples: the  $\text{TM}_{01}$  and  $\text{HE}_{21}$  modes at the 2<sup>nd</sup> harmonic and the  $\text{HE}_{12}$  and  $\text{HE}_{31}$  modes at the 3<sup>rd</sup> harmonic. Complex amplitudes  $\tilde{E}$  at the entrance for higher-order modes were set zero.

It is obvious that two different physical situations are possible with the dominance of the  $\text{HE}_{11}$  mode, in which the RF drive signal enters the interaction space. At the output cross-section, its power can be either prevailing or not prevailing over powers transmitting in higher-order modes at harmonic frequencies. In the first case, the antenna-amplifier device would operate like a conventional relativistic TWT, just with the specific, asymmetric operating mode that is suited for the drive signal input and output radiation extraction. In the second case, an unusually high RF power would be in harmonics that is more complicated compared to a traditional TWT, however, would represent a very interesting feature if the harmonics content in the output signal spectrum can be controlled electronically. The first case is more appropriate for initial experiments that would prove the concept of antenna-



amplifiers; the second case promises novel tuning schemes (tuning the ratio of harmonic amplitudes in the radiation spectrum), so that it can be considered for possible future research on the antenna-amplifier.

Therefore, our 1-D multimode simulations were aimed at finding the characteristic sets of parameters providing these two physical situations. In addition, for the first case, we determined the achievable efficiency of the device and for the second case, we focused rather on possible means to control electronically the harmonics content.

In Fig.2, the results of simulations are shown for the set of parameters that exhibited in [8] the significant prevalence of the fundamental mode over the higher-order ones in the linear growth rate. In these simulations, the initial condition for the dimensionless complex amplitude of the  $HE_{11}$  mode was  $\tilde{E} = (0.1, 0)$  for both positive and negative azimuthal index, meaning that the input signal was linearly polarized. This input signal induced frequency harmonics in higher-order modes, the level of which is seen from the plots\*. For the left plot, the main (input) frequency was set in the way providing the exact synchronism between the beam and  $HE_{11}$  mode phase velocity, i.e., the mismatch parameter  $\delta$  was zero for the  $HE_{11}$  mode. One can see that at the exact synchronism, the 2<sup>nd</sup> harmonic level is rather high. Even at the maximum of the main signal power ( $z \approx 19$  cm), where the efficiency reaches  $\sim 23\%$ , the 2<sup>nd</sup> harmonic level is just 10 dB less, and at longer lengths, where the main signal gets minimums, it becomes comparable and even exceeding (as one should add the powers of the  $TM_{01}$  and  $HE_{21}$  modes).

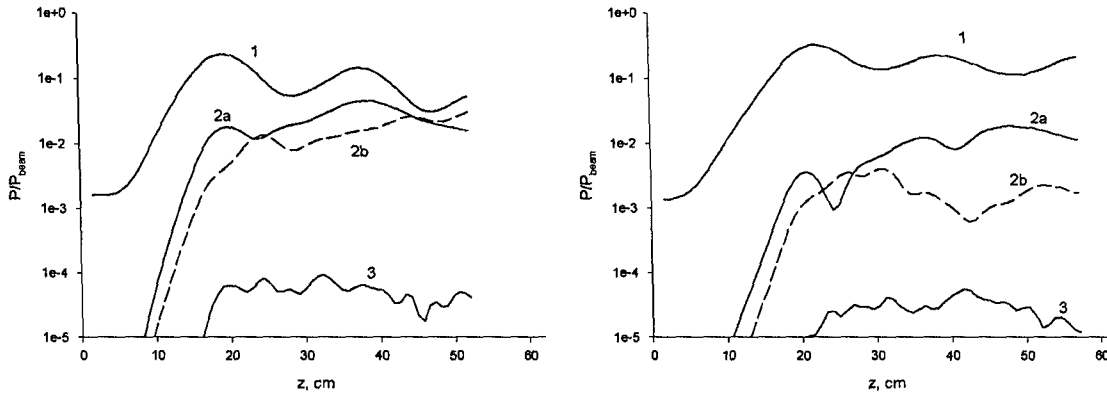


Fig.2. Microwave power of different modes vs. axial coordinate: 1 –  $HE_{11}$  mode at the main frequency; 2a –  $TM_{01}$  mode at the 2<sup>nd</sup> harmonic; 2b –  $HE_{21}$  mode at the 2<sup>nd</sup> harmonic; 3 –  $HE_{31}$  mode at the 3<sup>rd</sup> harmonic. The main frequency is 8.87 GHz (left) and 9.55 GHz (right).  $\varepsilon = 5$ ,  $a = 0.6$  cm,  $b = 2$  cm,  $r_b = 1$  cm,  $\gamma = 1.4$ ,  $I = 1$  kA.

For the increased drive frequency giving the positive mismatch, as is seen from the right plot in Fig.2, the simulation demonstrates well-known behavior of the main signal power; the maximum efficiency increases (up to  $\sim 32\%$ ) as well as the corresponding axial coordinate (up to  $\sim 22$  cm). An important thing here is that the harmonics power level significantly decreases; the difference from that of main signal makes  $\sim 20$  dB at its maximum and remains greater than 10 dB even at almost 3 times longer interaction space, which is evidently not applicable in practice. The power transmitted in the  $HE_{21}$  mode reduces in stronger degree compared to that in the  $TM_{01}$  mode.

Further increasing input frequency results already in suppression of the 2<sup>nd</sup> harmonic growth in both  $TM_{01}$  and  $HE_{21}$  modes. This can be seen from Fig.3 where its power level is at least 20 dB lower than the power in the operating  $HE_{11}$  mode over the whole simulation length. At the same time, further increasing mismatch for the  $HE_{11}$  mode does not lead to

\* For the  $HE_{12}$  mode, the curves are not shown since their level is too low.

significant increasing maximum efficiency and corresponding coordinate. In Fig.3, the maximum efficiency reaches  $\sim 33\%$  at  $z \approx 26$  cm. It should be noted here that the input power corresponding to the value of the dimensionless complex amplitude at  $z = 0$  is of  $\sim 270$  kW.

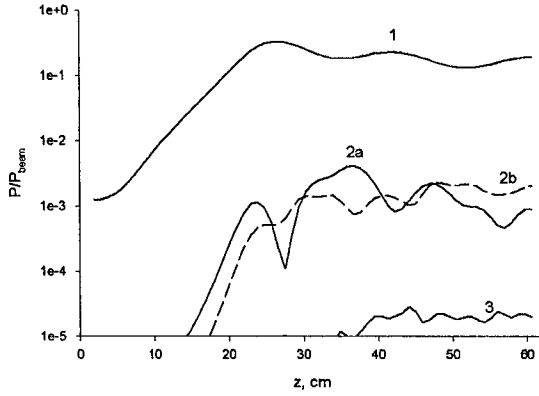


Fig.3. The same as in Fig.2 except for 9.9 GHz main frequency.

One can conclude from the results presented that the set of parameters taken for these simulations seems quite appropriate for initial proof-of-principle experiments on an X-band antenna-amplifier device.

Obviously, other parameters also can provide the dominance of the  $HE_{11}$  mode and main frequency in the output spectrum of X-band antenna-amplifier. For instance, simulations with a higher dielectric constant of the rod material demonstrate the same low level of power at harmonics, and the amplifier efficiency and optimal length remain close to shown in Figs.2-3.

However, in order to keep the operating frequency at the same level, one need to decrease the beam energy rather significantly. In particular, for  $\epsilon = 6$ , the proper value of Lorentz factor  $\gamma$  is as low as 1.25, so that the electrons energy ( $\sim 125$  keV) is almost twice lower than in the case of  $\epsilon = 5$ ,  $\gamma = 1.4$  ( $\sim 200$  keV). Therefore, the output power at such parameters would be almost twice lower too. On the other hand, with a lower dielectric constant, higher electrons energy is needed. For  $\epsilon = 4$ , the proper value of  $\gamma$  is 1.65 that corresponds to  $\sim 325$  keV. Such increasing operating voltage would make a device less compact, though, of higher output power.

Some results of 1-D simulations with  $\epsilon = 4$  are presented in Fig.4. As is seen from the left plot, increasing electrons energy leads also to increasing harmonics level. For the parameters of right plot, the same operating frequency is achieved again with  $\gamma = 1.4$  at the expense of the rod radius increase from 6 to 8 mm. This plot again exhibits a low harmonics level and maximum efficiency for the main signal of  $\sim 29\%$ ; though, the maximum is reached at considerably longer length ( $\sim 34$  cm) compared to the case of  $\epsilon = 5$  and thinner rod.

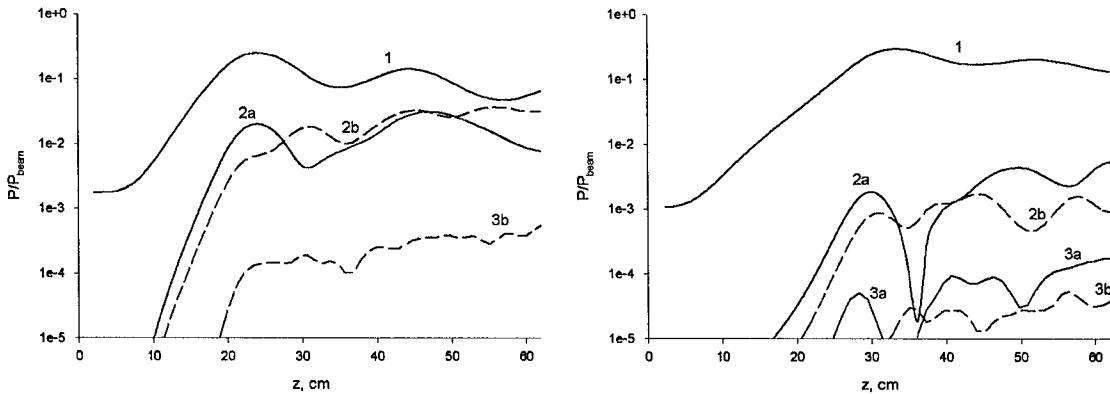


Fig.4. Simulation results for  $\epsilon = 4$ . The drive frequency is 9.4 GHz. The curves for modes growing at the 3<sup>rd</sup> harmonic are designated as: 3a –  $HE_{12}$  mode; 3b –  $HE_{31}$  mode. For the left plot,  $\gamma = 1.65$ ,  $a = 0.6$  cm,  $r_b = 1$  cm; for the right plot  $\gamma = 1.4$ ,  $a = 0.8$  cm,  $r_b = 1.2$  cm. Other parameters and designations are the same as in Fig.2.

An increase of the beam current also results in increasing harmonics level. For instance, for the parameters of the right plot of Fig.2, the twice-higher current of 2 kA yields almost

twice-higher power at 2<sup>nd</sup> harmonic in the TM<sub>01</sub> mode at the maximum of main signal power, whereas the efficiency increases very slightly. At the same time, if the current is varied within the range of 1.0-1.3 kA, the results of computation remain practically the same as plotted in Fig.2. It should be noted here that our assumption ignoring non-synchronous fields of the ac space charge might lead to a serious inaccuracy at high current values.

At last, the influence of the beam-rod gap, i.e., the coupling parameter, on the results of simulations is illustrated in Fig.5. Compared to the case of Fig.2, where the gap was 4 mm, it was taken 2 mm smaller (left plot) or 2 mm larger. It is seen that in case of strong coupling, the maximum power of the main signal is reached at considerably shorter length; however, the harmonics level is much higher than that shown in the right plot of Fig.2. In case of weak coupling, the harmonics level is, on the contrary, much lower, however, the main signal power is also a bit lower, and much longer rod is required to get its maximum. Evidently, the intermediate case of Fig.2 would be preferable for practical realization of the device.

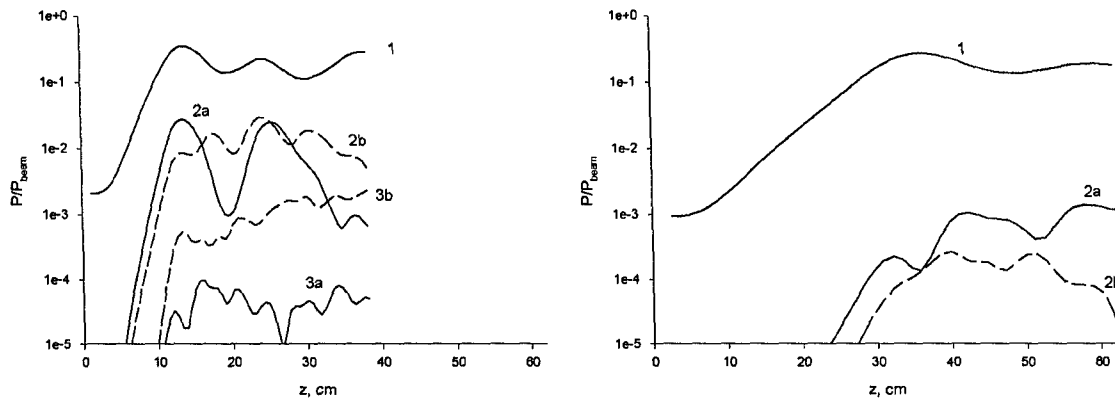


Fig.5. The same as in Fig.2 (the frequency is 9.55 GHz), except for  $r_b = 0.8 cm$  (left) and  $1.2 cm$  (right plot).

Thus, the following set of parameters was chosen for further particle-in-cell simulations and designing the initial gain demonstration experiments with the antenna-amplifier:  $\epsilon = 5.0$ ,  $a = 0.6 cm$ ,  $b = 2 cm$ ,  $r_b = 1 cm$ ,  $\gamma = 1.4$ ,  $I = 1.0-1.3 kA$ .

The effect of harmonic generation is strongly expressed for the parameters giving no prevalence in linear growth rate to the HE<sub>11</sub> mode over higher-order modes [8]. In Fig.6, the results of multimode simulations are shown for this set of parameters. The initial conditions for the HE<sub>11</sub> mode complex amplitude were taken, as for the previous set,  $\tilde{E} = (0.1, 0)$  for both  $l = \pm 1$  simulating the linearly polarized signal. This corresponds to the input microwave power of  $\sim 1.3 MW$ .<sup>\*</sup> For the left plot of Fig.6, the drive frequency corresponds to the exact synchronism with the beam; for the right plot, there is some positive mismatch.

It is seen that both plots exhibit a real mode competition between the fundamental HE<sub>11</sub> mode, TM<sub>01</sub> mode at the 2<sup>nd</sup> harmonic, and HE<sub>12</sub> mode at the 3<sup>rd</sup> harmonic. Microwave powers at harmonics become comparable and much exceeding the power at the main frequency, depending on the axial coordinate. It is important that the efficiency level seen here is absolutely typical for relativistic TWTs, and the length scale is quite reasonable to be realized in practice. In fact, the curves in Fig.6 represent dependences of powers in the modes involved into the competition process on the length of the interaction space. In the configuration with the beam propagating outside the inner rod, it is rather simple to control the point of beam removal out of the interaction space by changing the length of the guiding magnetic field. One can see that the variation of the place of beam dump over the range of only about 20 cm leads to a dramatic change of the output signal harmonics content. Indeed,

<sup>\*</sup> Such amount is quite accessible practically, if an X-band pulse compressor is used as microwave drive source.

different coordinates correspond to different situations. At  $z \approx 25$  cm, there is the dominance of the main frequency with the efficiency of 15-18%, while the efficiencies at the 2<sup>nd</sup> and 3<sup>rd</sup> harmonics do not exceed 4%. At  $z \approx 35$  cm, one can see, in fact, equal powers at the 1<sup>st</sup>, 2<sup>nd</sup>, and 3<sup>rd</sup> harmonics in the right plot, or rather close powers around  $z = 35$  cm in the left plot, with ~5-7% efficiency in each harmonic. At last, for  $z \approx 45$  cm, one has the dominance of the 2<sup>nd</sup> harmonic (~13-15% efficiency) with the 3<sup>rd</sup> harmonic middle and the main frequency lowest power (in the right plot, it falls even lower than the level of input signal). Hence, variation of the guiding magnetic field length, which can be realized, for instance, as turning on some reverse field coils placed above a main solenoid, represents a means of electronic control of the spectrum of output radiation, i.e., tuning the harmonics content.

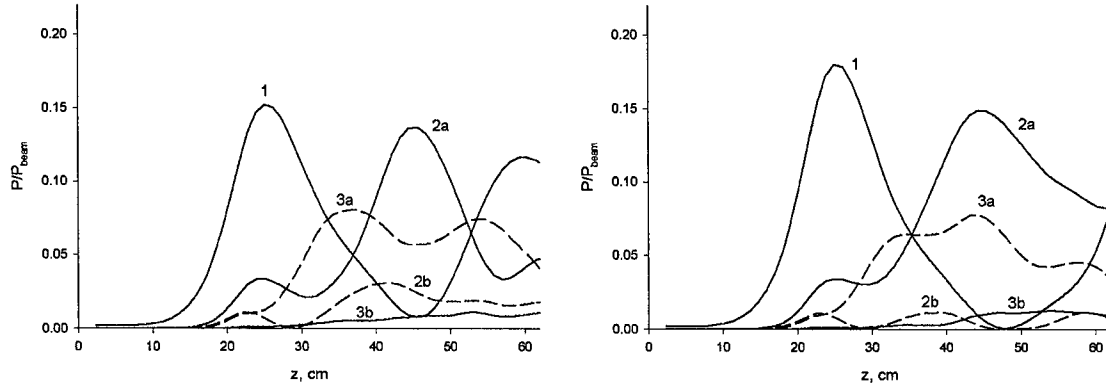


Fig. 6. Microwave powers vs. axial coordinate: 1 – HE<sub>11</sub> mode (main frequency), 2a – TM<sub>01</sub> mode, 2b – HE<sub>21</sub> mode (both at 2<sup>nd</sup> harmonic), 3a – HE<sub>12</sub> mode, 3b – HE<sub>31</sub> mode (both at 3<sup>rd</sup> harmonic). The main frequency is 9.38 GHz (left) and 9.9 GHz (right).  $\epsilon = 2.25$ ,  $a = 1$  cm,  $b = 2$  cm,  $r_b = 1.2$  cm,  $\gamma = 1.8$ ,  $I = 1.7$  kA.

The similar tuning can be achieved by means of the variation of input signal frequency as well. The linear gain-bandwidth is larger for the HE<sub>11</sub> mode than for other modes, so that for a large enough mismatch, the multiple frequencies may not reside within higher-order modes amplification bands any more. In Fig. 7, the results of simulations are plotted for higher drive frequencies giving ever increasing positive mismatch. For the main signal, the maximum efficiency increases up to 20-25% as expected, and the power level induced at harmonics decreases (as is seen from the right plot, the HE<sub>11</sub> mode already 'wins' the mode competition). Simulations show that the main signal can dominate over harmonics at a negative mismatch as well, but with less efficiency. The drive signal frequency variation can be easily realized, so that one can control harmonics content at a fixed length of the interaction region.

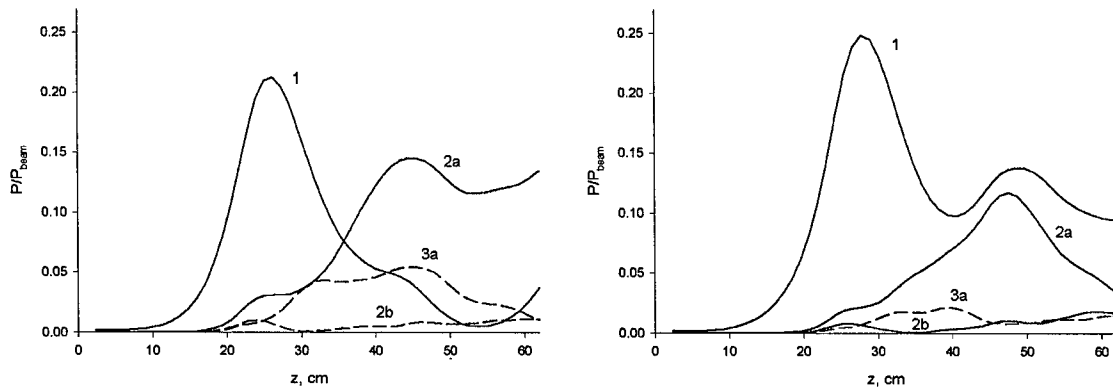


Fig.7. The same as in Fig.6 except for the main frequency is 10.5 GHz (left) and 11.33 GHz (right plot).

Also, there is a way to change the ratio of harmonic amplitudes in radiation spectrum at a fixed system length and input frequency both. Namely, the output signal spectrum can be

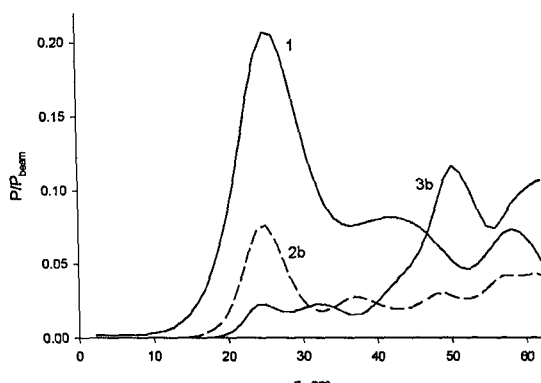


Fig.8. The same as in Fig.6 (left plot) except for the input signal polarization is circular.

'switched over' if the drive signal polarization is changed from linear to circular. Indeed, if the drive signal field pattern rotates, all particles are on average 'equal' regardless of their azimuthal positions; hence, bunching at different azimuths requires the same length, just bunches are formed around different phases. This means that the beam becomes looking like a regular helix, and only such modes can grow that have the same *angular* phase velocity as of the  $HE_{11}$  mode, i.e., the  $HE_{21}$  mode at the 2<sup>nd</sup> harmonic and the  $HE_{31}$  mode at the 3<sup>rd</sup>. The  $TM_{01}$  and  $HE_{12}$  modes cannot grow, unlike the case of linear polarization. An example of multimode

simulation performed with such initial conditions that  $\vec{E} = (0.1, 0.1)$  for  $l = 1$  and  $\vec{E} = (0, 0)$  for  $l = -1$ , which keep input power the same just setting the circular polarization for the drive signal, is presented in Fig.8. It is seen from the comparison with the left plot of Fig.6 that changing polarization represents one more means for electronic control of the harmonics power.

Thus, the investigated set of parameters  $\{\varepsilon = 2.25, a = 1 \text{ cm}, b = 2 \text{ cm}, r_b = 1.2 \text{ cm}, \gamma = 1.8, I = 1.7 \text{ kA}\}$  exhibited effective multiplication of X-band drive signal frequency in the antenna-amplifier due to the 2<sup>nd</sup> and 3<sup>rd</sup> harmonics generation, and our 1-D simulations demonstrated real possibilities for the output signal harmonics content to be controlled electronically. It means that novel tuning schemes can be realized. A device capable of tuning the ratio of harmonic amplitudes in the radiation spectrum consisting of several harmonics could find interesting applications. It seems important therefore to verify the existence of the effect discussed in full-scale 3-D particle-in-cell simulations. This feature of the antenna-amplifier is worthy of thorough experimental research in the future.

### b) 3-D particle-in-cell simulations

According to the above Section, there are two characteristic sets of parameters for the dielectric rod and electron beam in the antenna-amplifier, which are of interest for further investigations. Let us call them Set 1 and Set 2; they correspond to the discussed above cases of the  $HE_{11}$  mode dominance, or no dominance, respectively. We have carried out the full-scale numerical simulations of the antenna-amplifier device for both configurations using the 3-D version of the PIC code MAGIC. Simulations with the parameters of the Set 1 and Set 2 were, accordingly, aimed at different objectives.

For the Set 1, the main goal was in studying amplification (gain and bandwidth) with the geometry of the electron diode close to that of real model experiments on beam transport (see below) and possible future proof-of-principle experiments. Also important, in the light of experiments, was to get an idea about the value of electric field along the dielectric rod surface inside the annular electron beam. The configuration of the simulation space is presented in Fig.9.

The boundary in radial direction is formed by the conducting anode (30 mm radius) and drift tube (20 mm radius) with the tapered buffer section of 26 mm length in between. Inside the cathode of the coaxial diode, the dielectric rod (6 mm radius,  $\varepsilon = 5$ ) is inserted. At the left

boundary, two ports are set: outer (with respect to the conducting cathode) for a voltage applied, and inner for a microwave input. The right boundary was set as FREESPACE. The EMISSION EXPLOSIVE command was used to set particles emission. The emitting edge of

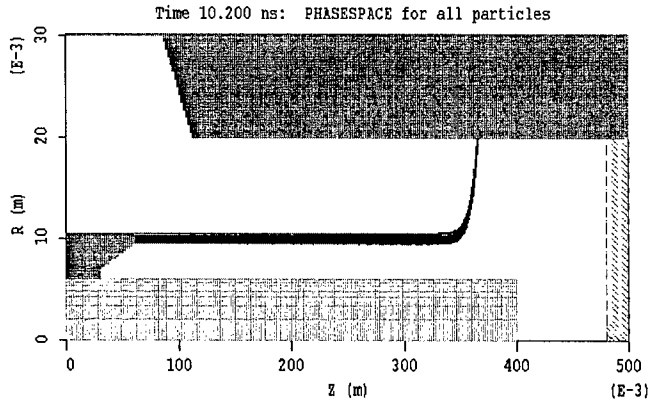


Fig.9. System geometry and beam axial cross-section.

the cathode is of 1 mm thickness and 10 mm mean radius; its axial coordinate was 6 cm in all simulations. Tapered region inside the cathode is the same as used in our model experiments; the rest of cathode geometry is simplified. The voltage set at the left boundary was adjusted in such a way that electrons Lorentz factor in the drift tube was close to  $\gamma = 1.4$  providing the beam current of 1.0-1.3 kA. Thus, the parameters were close to those of the Set 1. The beam was guided

by a strong preset magnetic field (3.0 T), so that the interaction region length was determined by the length of this preset field. As seen from Fig.9, this length is  $\sim 25$  cm. The input X-band signal was injected from the left into the waveguide of 6 mm radius totally filled with the dielectric in its fundamental  $TE_{11}$  mode, which excited (being very similar in field pattern) the  $HE_{11}$  mode of the dielectric rod. The signal was linearly polarized, i.e., the  $TE_{11}$  mode field pattern was fixed in time keeping purely radial electric component along the horizontal line (azimuthal coordinate  $\varphi = 0$ ). Typical run time for simulations was 10.2 ns.

Some results of simulation without a microwave input signal are presented in Figs.10-12 (for this case, the magnetic field length and entire simulation space were taken 10 cm shorter). Fig.10 shows the diode voltage level providing the required level of beam current. Electrons energies are plotted in Fig.11 (left). It is seen that at the acceleration stage (the region from the cathode to the drift tube), the beam acquires a significant energy spread determined both by its finite thickness and explosive emission process. As expected, the phase space plot exhibits uniformity beginning from the place located downstream of the entrance into the drift tube, at about the drift tube diameter. These factors influence on the amplifier efficiency.

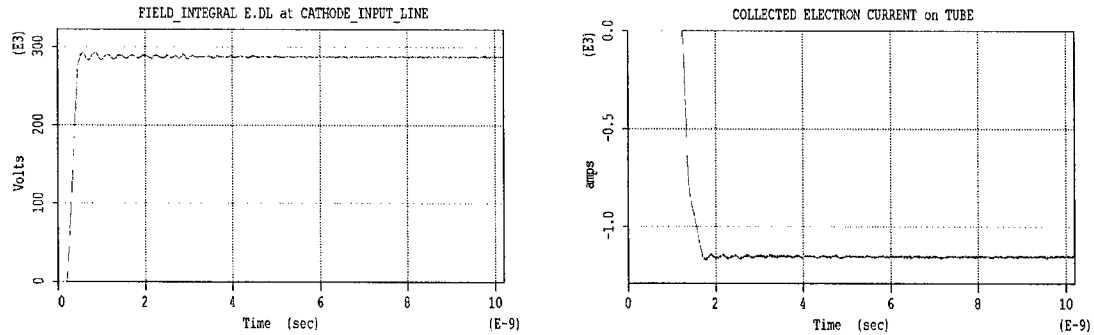


Fig.10. Diode voltage (left) and electron beam current collected on the drift tube (right plot). No RF input.

The right plot of Fig.11 shows the value of axial electric field component at the rod surface under the beam. It is practically absent in the region of beam phase space plot uniformity, since the dc space charge field inside a uniform annular beam is zero.  $E_z$  is non-zero in the region of acceleration and beam dump, and its actual values are important as this field may cause the surface breakdown along the rod. At the place of beam dump, as seen

from the plot,  $E_z \sim 15\text{-}16$  kV/cm that seems more or less acceptable. Its maximum value falls to  $\sim 3$  mm downstream of the cathode edge location and exceeds 60 kV/cm. This is much higher than the field in the region corresponding to the location of tapered buffer section, in which the breakdown was observed in our experiments. However, any breakdown traces on the rod under the cathode edge were not observed; this discrepancy remains unclear.

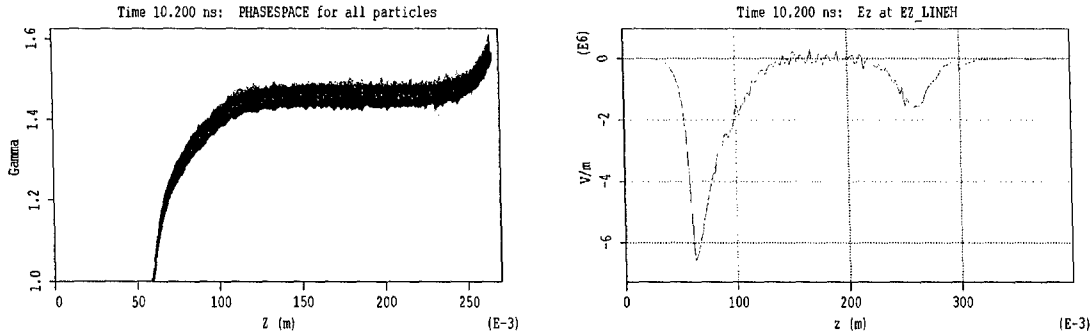


Fig.11. Beam phase portrait (left) and  $E_z$  field at the rod radius and  $\phi = 0$  vs.  $z$  coordinate (right). No RF input.

The radiation downstream of the rod produced in case of no RF input signal represents the beam noise as seen from Fig.12. The peak of  $\sim 60$  kW in the power time dependence corresponds to the moment of the beam head reaches the dump place. After that, the power falls down to several kilowatts. The spectrum is noisy, nevertheless, the maximum falls to the X-band as expected.

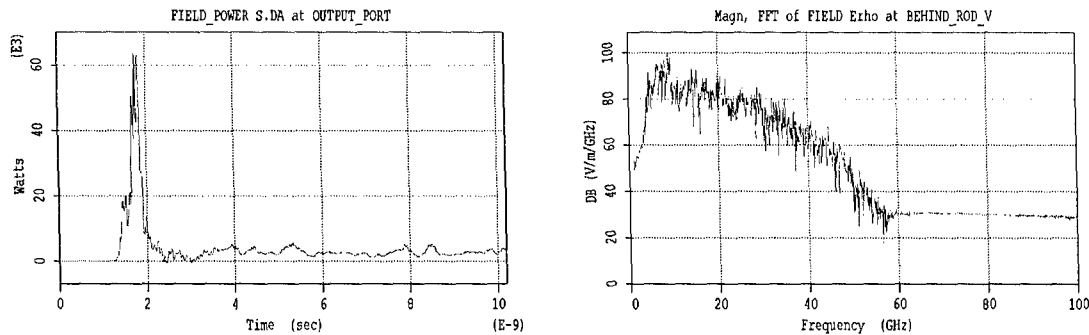


Fig.12. Output power (left) and FFT for radial electric field (right) at 8 cm behind the rod. No RF input.

When the input microwave signal of proper frequency enters the inner port at the left boundary, electron beam bunching is observed, and amplification takes place. Simulations performed at different frequencies have shown the maximum gain at 9.3 GHz. In Figs.13-16, some results of the simulation at 9.3 GHz are presented. Beam bunching is clearly expressed in Fig.13. The input power plotted at the right is obtained by integrating Poynting flux over the inner waveguide cross-section. Some decrease in the observed power near the input appears due to reflection from the rod end, since the dielectric constant is sufficiently high, and no matching was set. The gain is seen from Fig.14, where the output power obtained by integrating Poynting flux over the drift tube cross-section downstream of the beam dump location is plotted. Also, one can see here the difference in power before and behind the rod end caused by reflection. For gain estimations, we will use the power obtained in the cross-section including dielectric, upstream of its end, because in the real antenna-amplifier geometry, dielectric extends out of vacuum space. Thus, comparing the output power in the left plot of Fig.14 (its maximum value exceeds 10 MW) to the input power of  $\sim 210$  kW (Fig.13), one can conclude that maximum gain at the given beam length for the frequency of 9.3 GHz reaches  $\sim 17$  dB.

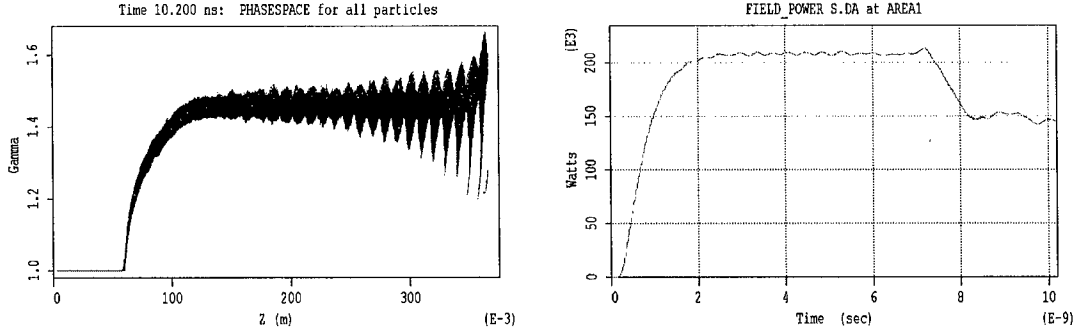


Fig.13. Beam phase portrait in case of 9.3 GHz RF input. The input power in the inner waveguide (at 1 cm from the port) is shown at the right plot.

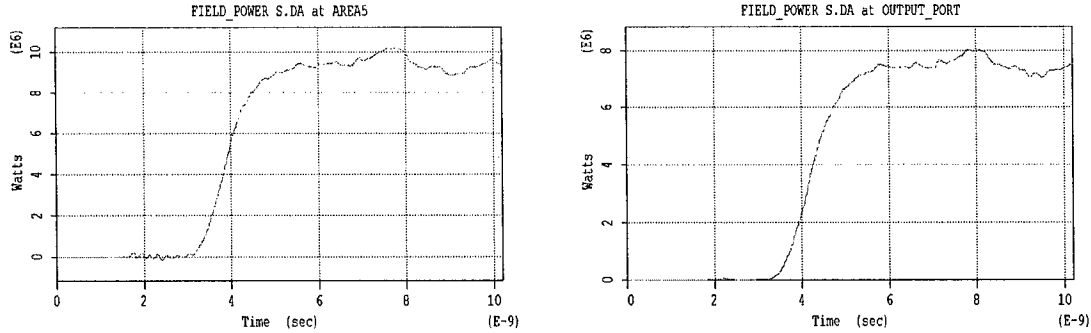


Fig.14. Output power vs. time in case of 9.3 GHz RF input. The observation cross-sections are at 1 cm before the rod end (left) and at 8 cm behind the rod end (right).

The radiation spectrum at the output is presented in Fig.15 as the FFT of the radial electric field time behavior for two points of different azimuthal positions, one corresponding to the input wave polarization and another one, at which the input wave has zero  $E_r$  component. It is seen that the peak corresponding to the drive frequency is much higher at the left plot; also, the rest of spectrum at the azimuth  $\varphi = 90^\circ$  is noisy whereas at  $\varphi = 0$ , frequency harmonics are clearly expressed. Evidently, the peak at the drive frequency in the point, where, for the  $HE_{11}$  mode having the polarization of the input signal,  $E_z = 0$  is associated with non-synchronous space charge oscillations. This is very well seen from the comparison of the plots showing  $E_z$  component profiles along the rod for these two azimuths, which are given in Fig.16. The field profile at  $\varphi = 90^\circ$  is similar to that obtained without RF input (Fig.11), whereas the profile at  $\varphi = 0$  associated with the amplified RF signal is extremely different. This field is even higher than the field under the cathode edge; in practice, though, breakdown along the rod at the device output can be eliminated at short enough RF drive pulse duration.

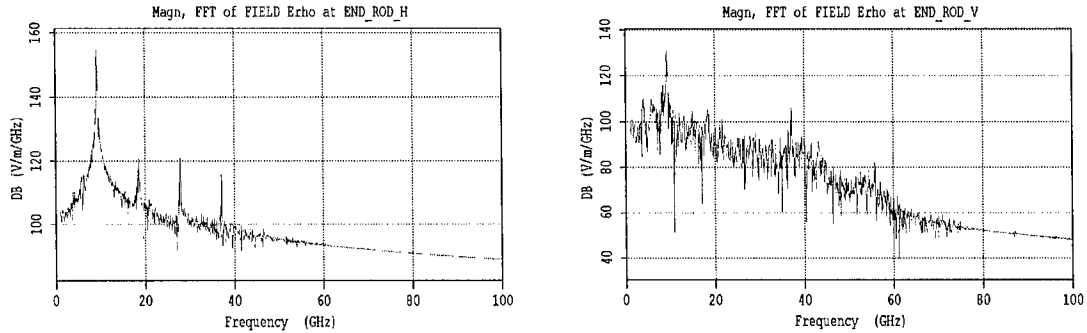


Fig.15. Output radiation spectrum (9.3 GHz RF input). The observation points are at the rod radius, 1 cm upstream of the rod end, and azimuths:  $\varphi = 0$  (left) and  $\varphi = 90^\circ$  (right).



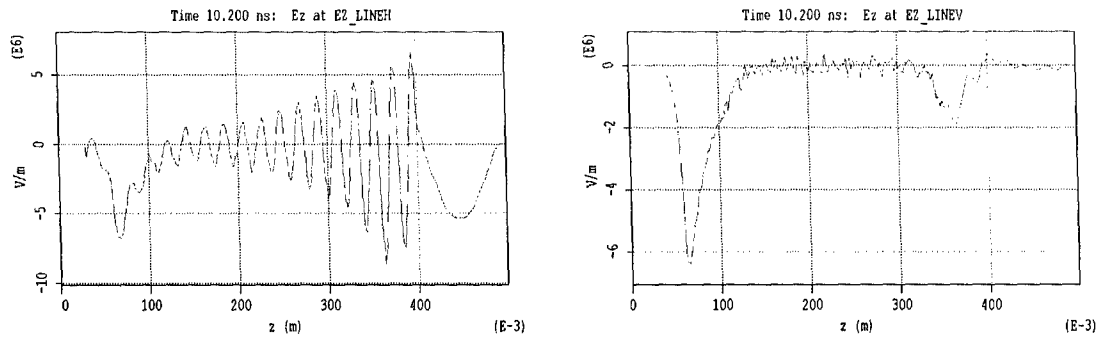


Fig.16.  $E_z$  field at the rod radius vs.  $z$  coordinate for  $\phi = 0$  (left) and  $\phi = 90^\circ$  (right). 9.3 GHz RF input.

In Figs.17-19, the results are shown illustrating the dependence of the output microwave power in the linear regime on the input signal frequency. The amplitude of the input signal was fixed, so that the input power was of  $\sim 210$  kW in these simulations. Comparing plots in Fig.17 with the left plot of Fig.14, one can conclude that the center of the amplification band falls to the frequency of  $\sim 9.3$  GHz. The simulation at 10.0 GHz already exhibits, in fact, no gain and bunching as one can see from Fig.18, especially, in comparison with the left plot of Fig.13. At the lower frequency of 8.6 GHz, which is symmetrically distanced, the gain and bunching are, nevertheless, still observed. From Fig.19, one can estimate that the gain is as low as  $\sim 11$  dB in this case.

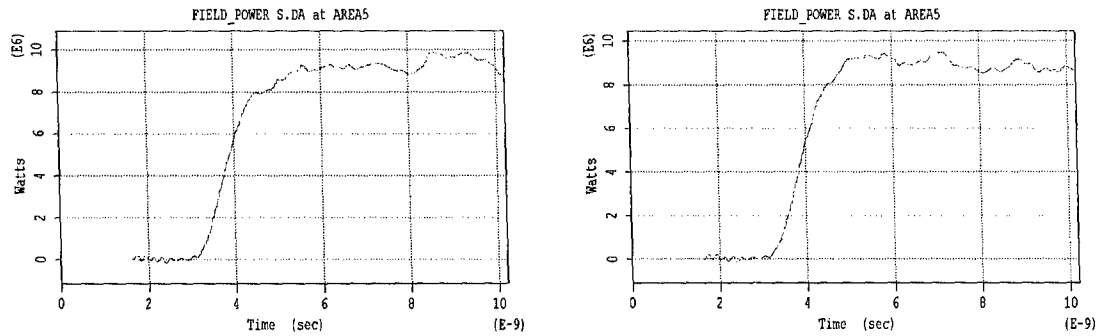


Fig.17. Output power (before the rod end) for 9.2 GHz (left) and 9.38 GHz (right) input frequency. Other parameters are the same as in Figs.13-16.

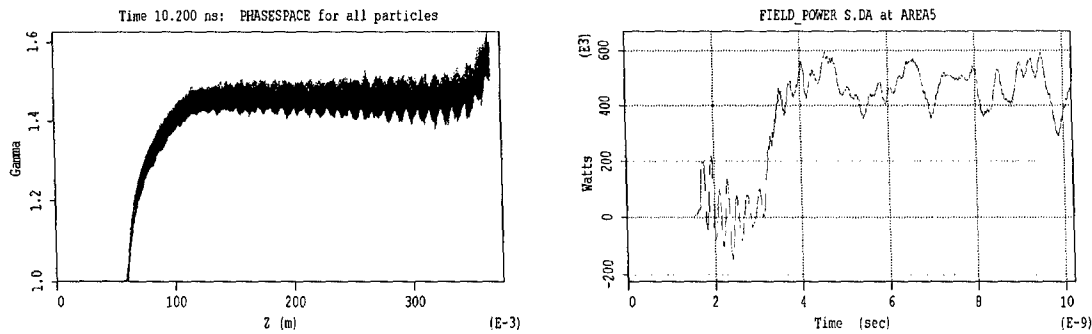


Fig.18. Beam phase portrait (left) and output power (right) in case of 10.0 GHz input frequency. Other parameters are the same as in Figs.13-16.

In the whole, one can conclude about the gain vs. frequency dependence that the maximum gain value is in good agreement with the linear theory, whereas the bandwidth turns out wider and shifted toward lower frequencies.

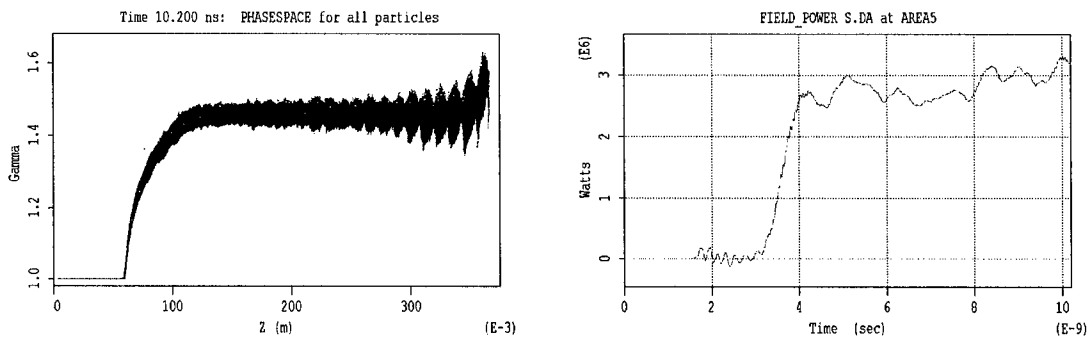


Fig.19. The same as in Fig.18 except for 8.6 GHz input frequency.

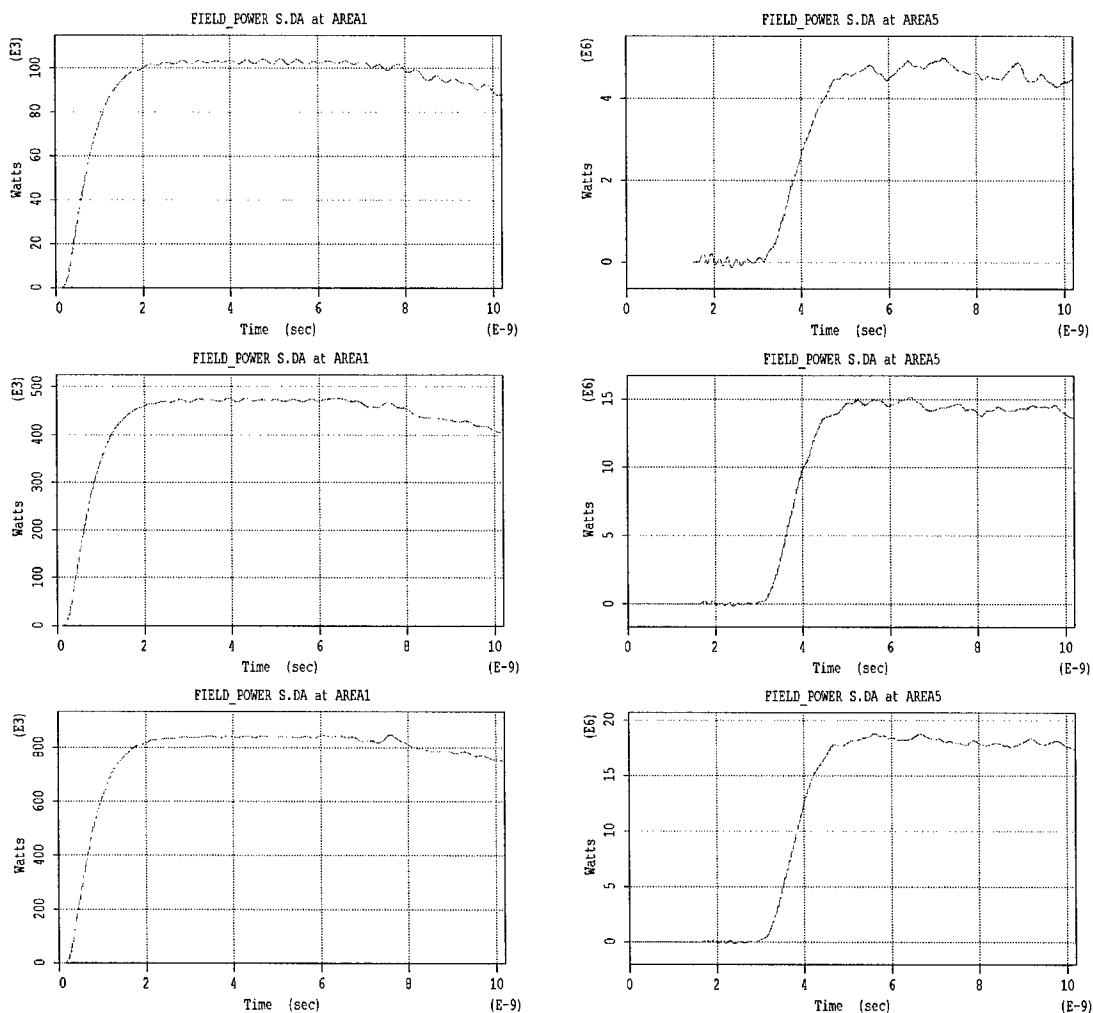


Fig.20. Output power (right plots) vs. input power (left plots) – nonlinear saturation. The frequency is 9.38 GHz.

In Fig.20, the simulations results showing the dependence of the output power on the input signal power are presented. Comparing the right top plot with the right plot of Fig.17 (for which the input power is twice higher), one can see the linear amplifier response at these input power levels. Deviation from linearity begins when the input power exceeds  $\sim 250$  kW level; the output power, correspondingly, exceeds  $\sim 10$  MW level. This is seen from the middle plots of Fig.20. For the bottom plots, the saturation manifests more than clear – the input power here is 8 times higher than for the top plots, however, the output power increases

only  $\sim 4$  times. In this case, the output power is close to the maximum at  $\sim 20$  MW level. That means the efficiency of the device reaches  $\sim 10\%$ . This is much lower than  $\sim 30\%$  obtained from 1-D simulations. The main reason for that is probably in the fact that the 1-D multimode theory does not take into account the non-synchronous fields of the ac space charge; also important is the abovementioned energy spread acquired by beam electrons at the stage of acceleration seen in 3-D simulations. Also, it should be noted that the harmonics level in case of maximum output power does not increase compared to that presented in Fig.15, i.e., it is even lower than obtained in 1-D simulations for the Set 1 demonstrating the dominance of the main frequency.

We have also investigated the influence of the dielectric rod tapering downstream of the beam dump place that eliminates reflections from the rod end. In addition, we placed the dielectric window across the simulation space upstream of rod tapering to simulate, in some sense, the real geometry of the antenna-amplifier device. The simulation geometry in this case is shown in Fig.21. The window of 4 mm thickness and  $\epsilon = 2.25$  was taken. It is seen from Fig.21 that the RF power at the input does not change with time, so that a reflected wave is absent, indeed (compare to the left middle plot of Fig.20, where simulation parameters are the same). This improves the gain, though, not significantly; the output power obtained at the same cross-section downstream of the beam dump as that in the right middle plot of Fig.20 increases only by  $\sim 1$  MW. The window practically does not affect the results of simulations.

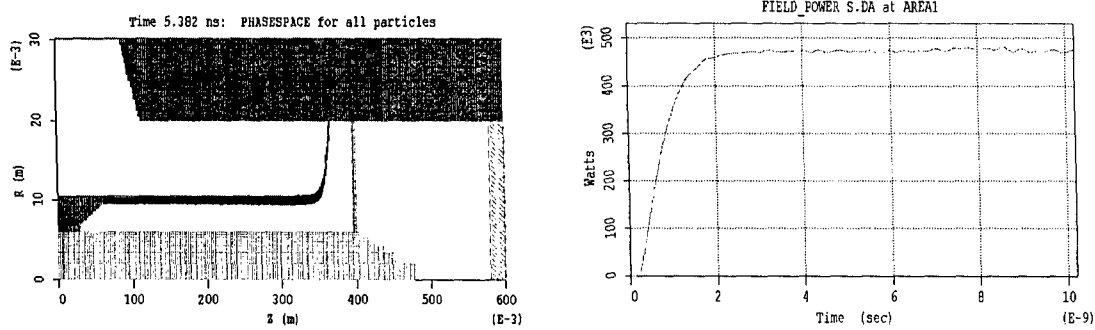


Fig.21. Geometry with matching and window (left) and power in the inner waveguide at 1 cm from the input port (right). The frequency is 9.38 GHz.

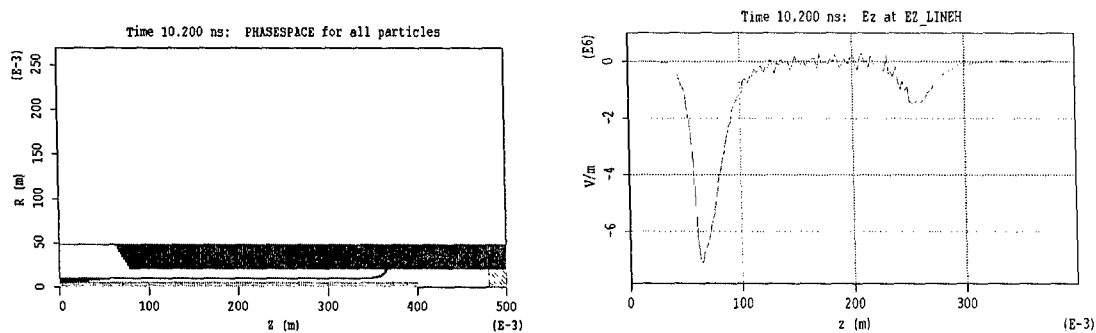


Fig.22. Quasi-planar diode geometry (left) and  $E_z$  field at the rod radius and  $\varphi = 0$  vs.  $z$  coordinate. No RF input.

At last, we have carried out the simulations with the diode geometry modified in the light of our experimental results showing that at the rod surface, breakdown occurs in the place located under the tapered buffer section. We tried, in fact, a quasi-planar geometry shown in Fig.22, where the cathode edge is much closer to the drift tube, instead of the coaxial diode. The outer radius was adjusted in the way providing the same beam current as presented in Fig.10. Comparing the  $E_z$  field profile along the rod surface obtained with no RF input signal,

which is shown in Fig.22, to that of Fig.11, one can see that the length of field drop after the peak it reaches under the cathode edge is considerably reduced. This may eliminate the surface breakdown. Simulations with the RF signal at the inner input port have given, in fact, the same results for the device gain. In comparison with the geometry of Fig.9, the length of electrons acceleration region is almost twice reduced. Hence, their interaction with the RF drive at this stage is usefulness, but not harmful.

Summarizing all results presented above, we conclude that the simulations performed for the parameters of Set 1 has allowed for planning future experiments on the gain demonstration. The amplification band found coincides with the frequency range of the available magnetron to be employed for microwave drive pulse production, and the output power level of 10-20 MW can be expected.

For the Set 2, the main goal was in verification of the new feature of the device found in 1-D simulations; therefore, idealized geometries and simplifying conditions were assumed. Initially, we used the EMISSION BEAM command as the simplest model of electrons emission. Later, we gave up this simplification and employed the EMISSION EXPLOSIVE command to simulate conditions in the electron diode and compare obtained results. In both cases, all conducting surfaces of cathode, anode, and drift tube were taken conformal in the cylindrical coordinate system. The geometries are shown in Fig.23.

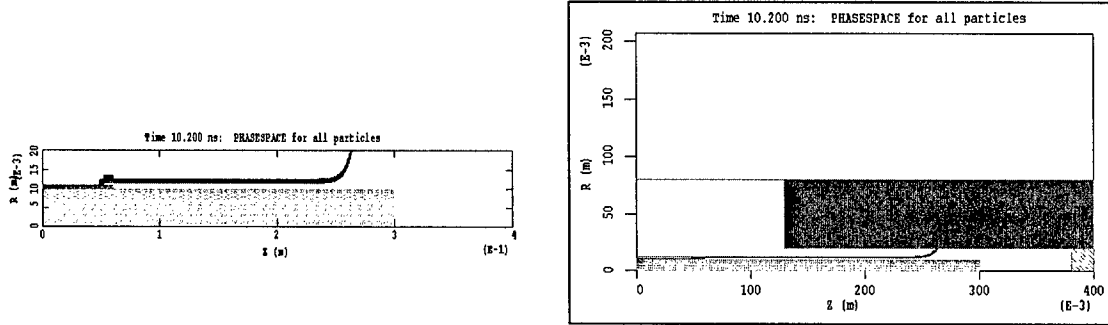


Fig.23. System geometries in simulations with the parameters of Set 2 using EMISSION BEAM command (left) and EMISSION EXPLOSIVE command (right).

The configuration presented in the right plot is, in fact, similar to that of Fig.9. The drift tube is of the same 20 mm radius. The inner waveguide (and dielectric rod) radius is 10 mm, the dielectric constant  $\epsilon = 2.25$ . The emitting cathode edge is of 12 mm mean radius; its thickness and axial position are the same as in simulations for the Set 1. The diode geometry and input voltage in the case of explosive emission were adjusted in the way providing the beam current and electrons energy (at the beginning of interaction) close to those of simulations using EMISSION BEAM command. In its turn, the system, for which the EMISSION BEAM command was used, has the same drift tube, cathode, and rod geometry, and the beam voltage of 500 kV provides  $\gamma \approx 1.8$  for particles Lorentz factor and the current level close to that of the Set 2. The outer part of the simulation space left boundary (at the left plot of Fig.23) was set as the right boundary, FREESPACE.

In the course of simulations, the gain and electron beam bunching in non-axisymmetric microwave fields have been demonstrated, the effect of drive signal frequency multiplication has been verified, and the possibilities to control harmonics content in the output signal spectrum have been confirmed. The possibility connected with the input frequency variation is illustrated in Fig.24 for the simplest case of EMISSION BEAM command. It is seen that changing the input frequency results in the second harmonic decreasing by almost 10 dB and the third harmonic increasing. At the same time, the output power remains unchanged at the level of  $\sim 60$  MW; it is the nonlinear regime with the efficiency of  $\sim 15\%$ . This result agrees satisfactorily with that obtained in 1-D simulations, because of the simplified model of

emission, which gives a small energy spread, and probably, less influence of the ac space charge fields compared to the case of Set 1 parameters. It should be noted also that in 1-D simulations only the 2<sup>nd</sup> and 3<sup>rd</sup> harmonics were taken into account, whereas in 3-D full-scale PIC simulations, one can see in the spectrum as many as six harmonics dominating over the noise.

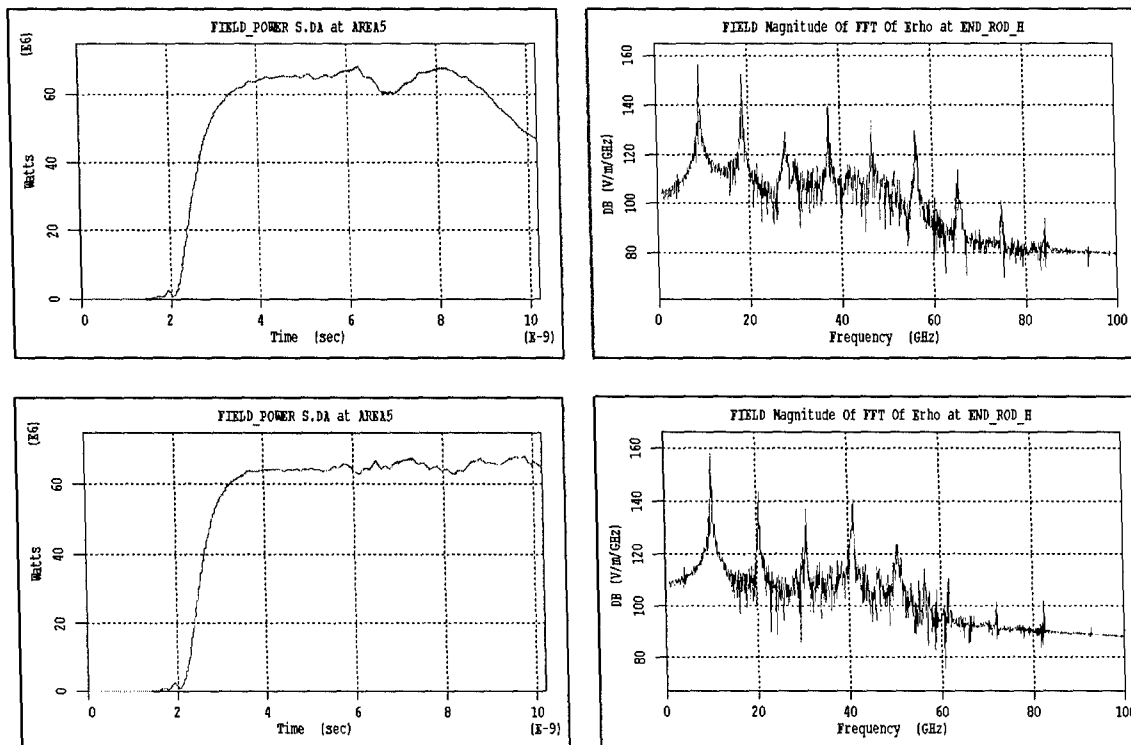


Fig.24. Output power vs. time (left plots) and FFT for radial electric field component at  $\varphi = 0$  (right plots). The interaction space length is increased by 10 cm compared to Fig.23 (30 cm from beam emitter to dump place). The input power is  $\sim 0.9$  MW. The frequency is: 9.38 GHz (top) and 10.3 GHz (bottom).

As to the influence of real conditions of electron emission in the coaxial diode, the key illustration is in Fig.25, where phase portraits demonstrating beam bunching are shown. Since a certain distance is required for particles acceleration up to the needed energy, a longer dielectric rod should be employed in the configuration using the model of explosive emission to achieve a similar level of bunching that is seen from the comparison of the left and right plots. The beam energy spread appears now at the stage of acceleration due to both the emission model and the influence of the RF drive signal (the latter is because the mentioned distance is longer than that required for the parameters of Set 1).

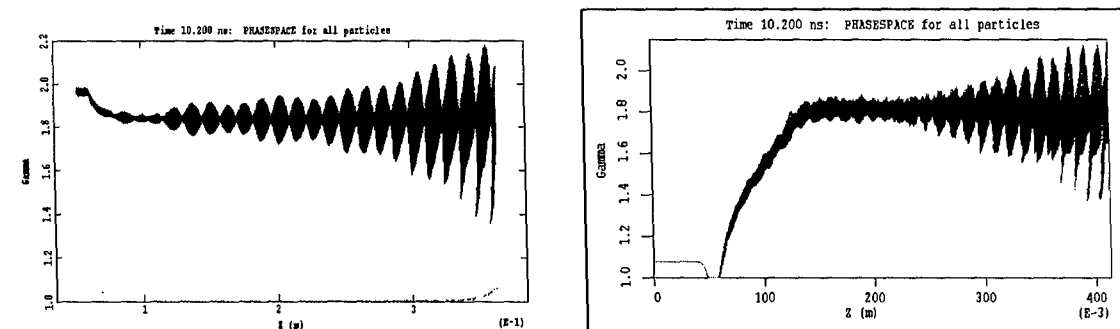


Fig.25. Particles Lorentz factor vs. axial coordinate for different models of emission: EMISSION BEAM command (left) and EMISSION EXPLOSIVE command (right).

This energy spread significantly influences on both the gain for the main frequency and the level of harmonics generation. The power and spectrum of the output signal obtained in simulations with the EMISSION EXPLOSIVE command are presented in Fig.26. Taking into account the distance between the cathode and entrance into the drift tube, the length of the interaction region is here close to that in simulations with the EMISSION BEAM command; nevertheless, the output power level of only  $\sim 30$  MW is achieved, i.e., twice lower than that computed with the simplified model of emission. In the spectrum, the noise level is considerably higher compared to the right top plot of Fig.24, and in fact, only the 2<sup>nd</sup> harmonic dominates over the noise.

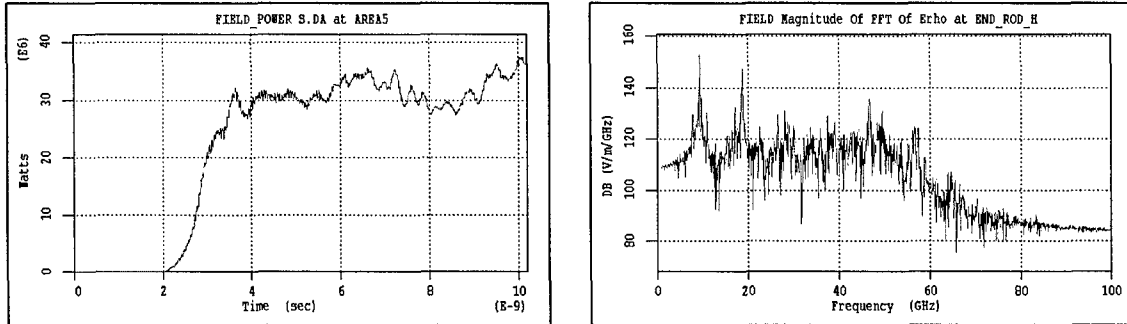


Fig.26. The same as in Fig.24 (top) for the system using the EMISSION EXPLOSIVE command in simulations and at the interaction space length increased by 15 cm compared to Fig.23.

One can finally conclude about the 3-D MAGIC simulations carried out with the parameters of the Set 2 that the effect of significant harmonics growth and the possibility of controlling harmonics content in the output spectrum found in the 1-D simulations have been confirmed. At the same time, further detailed investigations are necessary before designing experiments on the antenna-amplifier device realizing the tuning schemes discussed in the previous section.

### c) Linear theory for conducting, disc-loaded rod

The investigation of Cherenkov interaction for the case of annular beam in the waveguide with an inner periodic conducting slow-wave structure is of interest from the standpoint of comparison of achievable gain and bandwidth values with the case of an inner dielectric rod. Its aim is to make clear whether conducting surface wave antenna could be preferable for the antenna-amplifier device to be based on, since in the absence of dielectric, there are no problems connected with the near-surface plasma formation.

In this section, the linear theory is developed for the case of a disc-loaded rod antenna in a circular waveguide. Like a dielectric rod antenna, the disc-loaded conducting rod represents the well-developed kind of surface wave antennas [7]. The important difference is in the fact that for the system with the dielectric rod, the lowest, dipole  $HE_{11}$  mode is very well separated from other modes in frequency corresponding to a given phase velocity [8]. The system with the conducting rod, as a coaxial system, supports propagation of the axisymmetric quasi-TEM mode, which has no cut-off frequency like the TEM-mode of coaxial waveguide, but has an axial electric field component and a slight dispersion of slowed down phase velocity. This mode will be fundamental in the Cherenkov interaction with the electron beam; however, the non-axisymmetric  $HE_{11}$  mode of this system may have close frequencies of velocity synchronism that may lead to a strong mode competition.

The consideration below is carried out using the simplified model of infinitely small period of the system, i.e., not taking the space harmonics into account (one-wave

approximation). Under this assumption, non-axisymmetric modes having all six RF field components cannot be considered because for them, the axial magnetic field cannot be constant between the discs due to the boundary conditions at the disc surface. Therefore the initial consideration is limited by the case of azimuthal symmetry.

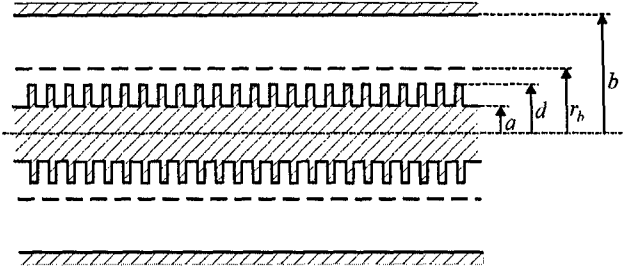


Fig. 27. Axial cross-section of the structure.

The geometry of the system is depicted in Fig. 27\*. The hollow electron beam is shown by the dashed line. It is assumed to be infinitely thin, fully magnetized, and monoenergetic.

In one-wave approximation, the RF fields in the region between two neighbor discs do not depend on the axial coordinate. Taking this into

account, one can find from the wave equation the following solutions for the axial electric field component as a function of the radial coordinate  $r$ :

$$E_z(r) = \begin{cases} E_0 \frac{F(ka, kr)}{F(ka, kd)}, & a \leq r \leq d \\ E_0 \frac{\Phi(qr, qr_b)}{\Phi(qd, qr_b)} + E_b \frac{\Phi(qd, qr)}{\Phi(qd, qr_b)}, & d \leq r \leq r_b \\ E_b \frac{\Phi(qr, qb)}{\Phi(qr_b, qb)}, & r_b \leq r \leq b \end{cases}$$

Here,  $k = \omega/c$ ,  $q^2 = h^2 - k^2$ ,  $\omega$  and  $h$  are the circular frequency and axial wavenumber,  $c$  is the speed of light,  $E_0$  and  $E_b$  are the field values at the radii of the disc edges and beam, respectively, and functions  $F$  and  $\Phi$  are defined as:

$$F(x, y) = J_0(x)Y_0(y) - J_0(y)Y_0(x), \quad \Phi(x, y) = I_0(x)K_0(y) - I_0(y)K_0(x),$$

where  $J_0$ ,  $Y_0$  are Bessel functions, and  $I_0$ ,  $K_0$  are modified Bessel functions of zero order.

These solutions are matched using the condition of the continuity of  $H_\phi$  field component at the radius of the disc edges and the condition for the derivative jump at  $r = r_b$  obtained from the linearized fluid equations for the beam [8]

$$\left\{ \frac{dE_z}{dr} \right\}_{r=r_b} = - \frac{2eI}{\beta\gamma^3 mc^3} \frac{q^2}{(k - \beta h)^2} \frac{E_b}{r_b},$$

where  $I$  is the beam current,  $\beta$  is its normalized velocity,  $\gamma$  is the Lorentz factor,  $m$  and  $e$  are the electron rest mass and charge.

Simple but tedious formula manipulations finally yield the dispersion relation of the system:

$$\left[ \frac{k \Phi(qb, qd)}{q \Phi(qd, qb)} - \frac{F'(ka, kd)}{F(ka, kd)} \right] \frac{(k - \beta h)^2}{\Phi(qr_b, qb)} = \frac{2q^2 I_b}{\beta\gamma^3 I_A} \frac{\Phi(qd, qr_b)}{\Phi(qd, qb)} \left[ \frac{F'(ka, kd)}{F(ka, kd)} - \frac{k \Phi'(qr_b, qd)}{q \Phi(qd, qr_b)} \right],$$

where

$$F'(x, y) = J_0(x)Y_0'(y) - J_0'(y)Y_0(x), \quad \Phi'(x, y) = I_0(x)K_0'(y) - I_0'(y)K_0(x).$$

\* It is interesting to note that the structure under consideration here was employed in the very first, pioneer experiment on high-power microwave generation [14].

The results of the numerical investigations of this dispersion relation are presented in Fig.28. Achievable values of gain and bandwidth in the quasi-TEM operating mode are well illustrated in comparison with those achievable in the structure with the dielectric rod in its lowest  $HE_{11}$  mode. The results of growth rate calculations plotted in Fig.28 were obtained for the same electron beam and the same radii of disc edges (for disc-loaded rod) and dielectric surface (for dielectric rod); the depth of grooves in the disc-loaded rod was varied.

For the left plot of Fig.28, the parameters of the beam and rod ( $d/b = 0.3$ ) correspond to the case of the  $HE_{11}$  mode domination in the instability spectrum presented in [8] for the system with the dielectric, i.e., to the Set 1 defined above. For the curve 1 in this plot, the depth of grooves is such that the peak gain frequencies in the cases of disc-loaded rod and dielectric rod (dashed curve) are very close. It is seen that for the disc-loaded rod, the gain is much higher and the amplification band is significantly wider than for the dielectric rod at all other parameters fixed. As the depth of grooves reduces (curve 2), the amplification band shifts to higher frequency, the relative bandwidth becomes narrower, and the peak gain decreases.

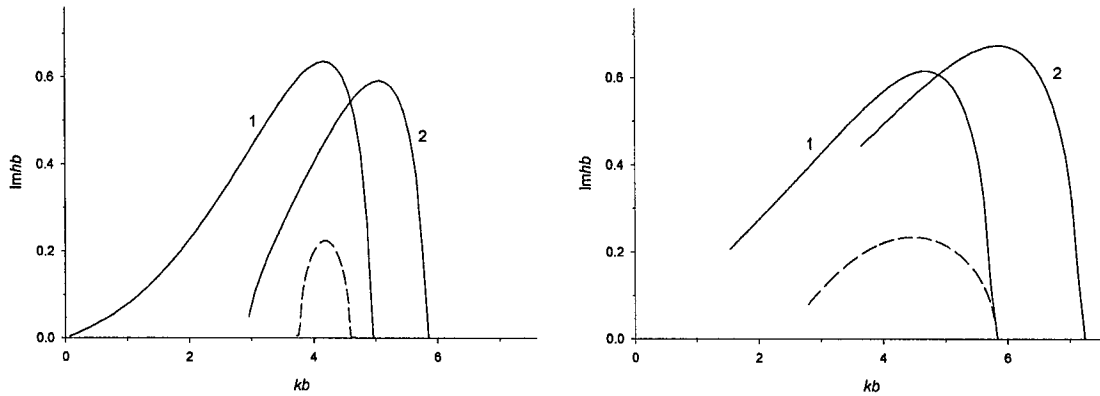


Fig.28. Spatial growth rates vs. frequency for the thin hollow beam propagating between the disc-loaded rod and circular waveguide (solid curves) in comparison with growth rates of the  $HE_{11}$  mode of the system with the dielectric rod (dashed curves). For the left plot,  $\gamma=1.4$ ,  $I = 1$  kA,  $r_b/b = 0.5$ ,  $d/b = 0.3$ ,  $a/b =$ : 1 – 0.15, 2 – 0.17, dielectric rod has the same radius  $d/b = 0.3$  and  $\epsilon=5$ . For the right plot,  $\gamma=1.8$ ,  $I = 1.7$  kA,  $r_b/b = 0.6$ ,  $d/b = 0.5$ ,  $a/b =$ : 1 – 0.375, 2 – 0.4, dielectric rod has the same radius  $d/b = 0.5$  and  $\epsilon=2.25$ .

The fact that much higher gains are achievable for the disc-loaded rod is naturally explained by stronger beam coupling to the synchronous mode at a given distance between the beam and rod surface. Indeed, the quasi-TEM mode is the mode of pure TM-type, whereas the  $HE_{11}$  mode of the structure with the dielectric rod is the hybrid mode originated from the  $TE_{11}$  mode of a circular waveguide, which has no axial electric field component; hence, the coupling impedance of the  $HE_{11}$  mode cannot be as high as that of the quasi-TEM mode. The wider bandwidth achievable with the disc-loaded rod can be explained by a significantly weaker dispersion of the quasi-TEM mode in comparison with the  $HE_{11}$  mode of the system with the dielectric rod. Indeed, the quasi-TEM mode has no cut-off frequency, and its phase velocity is always subluminal that is not the case with the  $HE_{11}$  mode.

For the dashed curve at the left plot of Fig.28, the dielectric constant is rather large ( $\epsilon=5$ ) that contributes into stronger dispersion. In the right plot, the comparison is made for the parameters corresponding to the Set 2, which give no prevalence for the  $HE_{11}$  mode of the dielectric-loaded structure in the instability spectrum. In this case, the dielectric constant is smaller, and it is seen that the bandwidths corresponding to the dashed and solid curves are of the same order. However, the peak gain remains higher for the case of disc-loaded rod in the same degree as for the parameters of the left plot.



It should be noted that, in difference of the left plot of Fig.28, reducing the depth of grooves at the parameters of the right plot does not result in decreasing peak gain, but on the contrary, the peak gain increases. This is due to higher beam energy and shorter beam-rod gap keeping the beam within the scale of evanescence of the surface wave even at the reduced wavelength corresponding to the velocity synchronism.

As is seen from the comparison presented above, the achievable gain in the quasi-TEM mode of the structure comprising the disc-loaded rod antenna and outer circular waveguide is much higher than in the  $HE_{11}$  mode of the waveguide with the dielectric rod. At the waveguide dimension giving the X-band operating frequency, the gain per unit length reaches  $\sim 3$  dB/cm. In addition, the bandwidth for the disc-loaded rod can be considerably wider under certain parameters. That means one could employ the conducting surface wave antenna to realize the concept of hybrid antenna-amplifier device.

Nevertheless, there are significant difficulties connected with the problem of the microwave drive signal input in the case of conducting rod antenna. As was said in the introduction, the key feature of the antenna-amplifier concept making the device compact is that a rod antenna feed waveguide serves, at the same time, as a hollow cathode holder of a diode producing a relativistic electron beam. Unlike the dielectric rod, the conducting rod should not be in contact with the cathode; otherwise the beam is not able to drift through the interaction space. If the rod were distanced from the cathode (i.e., the horn of antenna feed waveguide), it would result in reflection losses of the RF drive signal. One could use some insulating supports for the rod inside the cathode holder; in this case, there is a problem of possible emission from its inner surface.

Another factor contributing to the problem of RF drive input in the case of disc-loaded rod antenna is the excitation of the non-axisymmetric  $HE_{11}$  mode of this system mentioned above. To avoid a multi-mode transmission of the feed signal, it is more natural if it propagates in the  $TE_{11}$  mode of the circular feed waveguide. However, if the  $HE_{11}$  mode is operating, the competition of the quasi-TEM mode can be very significant.

In spite of these difficulties, a solution can be found allowing for the use of the conducting rod antenna in the antenna-amplifier device. Though, it requires additional investigations. It is of particular importance to develop the linear theory taking into account the space harmonics to consider the Cherenkov interaction of the beam with non-axisymmetric modes of the structure with the disc-loaded rod.

Thus, one can conclude from the above consideration and discussion that the decisive issue with regard to the question 'which kind of a rod antenna, dielectric or conducting, is preferable?' is anyway the model experiments on annular electron beam transport with the dielectric rod inside.

## 2. Task 2. Experimental exploration of the concept of antenna-amplifiers

### a) LIA module design

For our model experiments on annular electron beam transport with the dielectric rod inside and future proof-of-principle experiments on gain demonstration in the antenna-amplifier, we have designed, mounted, and launched the LIA module appropriate for the device. We have taken the abovementioned parameters of the Set 1 as input for the LIA design, i.e., the voltage of 260-290 kV and current of 1.0-1.3 kA (this gives the electrons Lorentz factor  $\gamma \approx 1.4$ ).

Compact LIAs in the Nuclear Physics Institute at Tomsk Polytechnic University are developed since the beginning of the 80s on the base of the original components: low-impedance strip pulse-forming lines and multi-channel spark gaps with forced current division into channels [15]. Significant LIAs' features are relatively low excitation voltage for one inductor and high efficiency of electrical energy transformation into relativistic electron beam energy.

The traditional scheme of the LIA providing its compactness employs the multi-channel spark gap for switching the strip forming lines wound around the induction system to discharge them through the turns surrounding the induction cores. The scheme modified to incorporate the elements of the antenna-amplifier is shown in Fig.29.

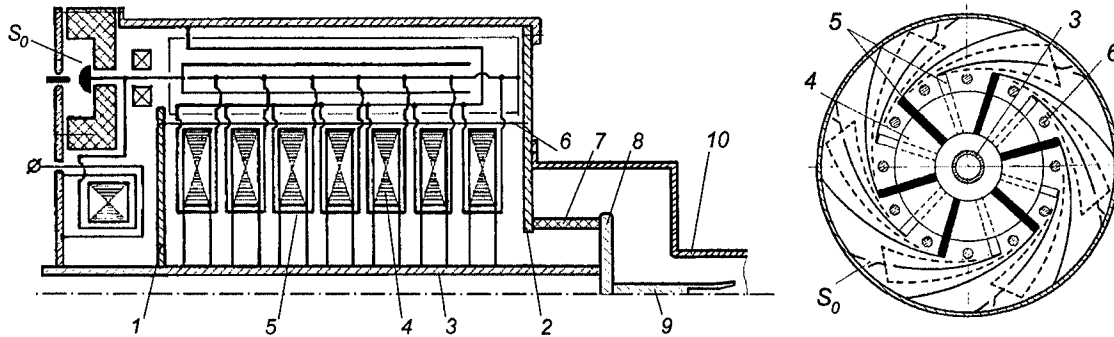


Fig.29. Schematic of the LIA module for the antenna-amplifier.  $S_0$  – multi-channel spark gap; 1,2 – flanges of induction system; 3 – hollow high-voltage electrode; 4 – ferromagnetic cores; 5 – magnetization turns; 6 – studs; 7 – insulator; 8 – high-voltage flange; 9 – cathode holder; 10 – anode of coaxial diode.

The induction system consists of seven ferromagnetic toroidal cores 4 pressed together by twelve studs 6 between the flanges 1 and 2. The studs, along with the central high-voltage electrode 3, form the turn, on which the electromotive forces of excitation of all the cores are added. The magnetization turns 5 surrounding the cores are connected to the electrodes of six double pulse-forming lines (PFLs) connected in parallel. Strip PFLs' electrodes are wound around the cores along a spiral of Archimedes. The potential electrodes are mounted at the common arm and connected to the anodes of multi-channel spark gap  $S_0$ ; the grounded electrodes are brazed to the inner surface of LIA tank.

The electrodes are made of copper foil; the insulation material is syntoflex. To reduce the electric field strength at the edges of electrodes, their contours are coated with the weakly conductive layer, which bulk resistance ( $\sim 10^6 \Omega \cdot m$ ) is  $10^4$ - $10^5$  times less than that of line insulation. The strip width is determined by the amount and dimensions of the induction cores; the length determining the voltage pulse duration is connected with the inner and outer diameters of winding and thickness of the strip and insulation. The resulting capacitance of the PFLs determines the capacitance of a primary storage to be used to charge the PFLs in a matched regime.

The accelerating voltage produced in the LIA is applied to the cathode of the coaxial magnetically insulated diode. For the cathode diameter of 20 mm (Set 1), the diameter of the anode 10 is 60 mm that provides the required level of the diode impedance in the required voltage range. The solid high-voltage flange 8 and cathode holder 9 shown in Fig.29 were used in the experiments on beam transport (the cathode holder was just made hollow in the end section for the dielectric rod to be inserted). For the future proof-of-principle experiments, the entire cathode holder is made hollow, as it is simultaneously the part of the microwave transmission system for an external X-band signal. This system is incorporated inside the LIA center high-voltage electrode as presented in Fig.30.

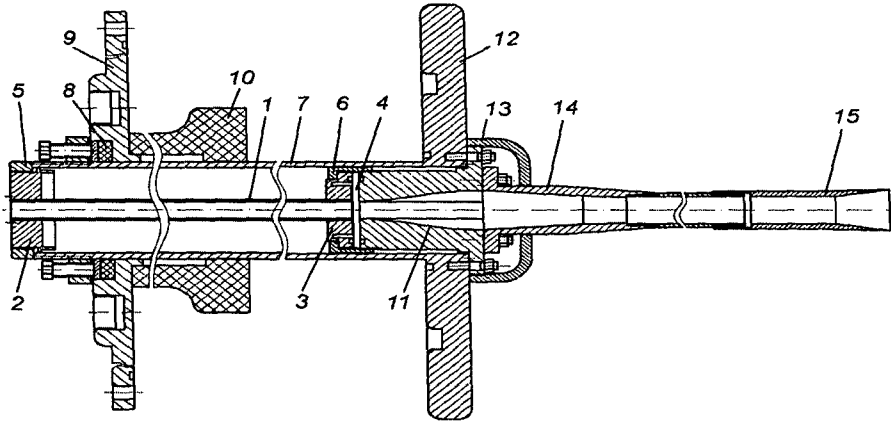
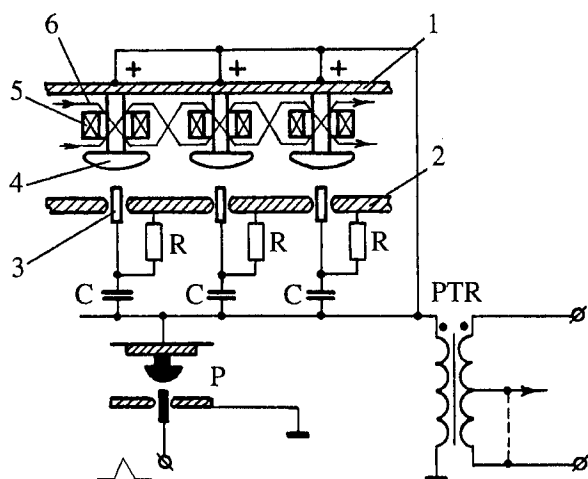


Fig.30. Microwave transmission system inside the LIA module (schematic). 1 – standard rectangular waveguide; 2,3 – waveguide flanges; 4 – vacuum window; 5,6 – fixing nuts; 7 – LIA center electrode; 8 – seal; 9 – end flange of LIA tank; 10 – support for LIA pulsed transformer; 11 – buffer section (rectangular-to-circular waveguide transformer); 12 – LIA high-voltage flange; 13 – rounded screen; 14 – cathode holder; 15 – cathode.

It is seen that inside the LIA center electrode 7, there are the standard X-band rectangular waveguide (23×10 mm) 1 and the buffer section 11 representing a rectangular-to-circular waveguide transformer. At the external, grounded side, the flange 2 and fixing nut 5 provide the contact with the center electrode and the end flange of LIA tank 9. The flange 2 is connected to the standard ninety-degree bend, so that an external source of X-band drive signal is placed sideways (this is not shown in the Figure). At the opposite end, the choke waveguide flange 3 with the vacuum window 4 is fixed by means of the coupling nut 6 at the buffer section 11, which is, in its turn, fixed at the LIA high-voltage flange 12 from the vacuum side. The cathode holder 14 is connected to the buffer section; the screen 13 shields these bolted joints. The inner surface of the cathode holder (and cathode 15) represents a waveguide transformer to the end waveguide finally exciting the  $HE_{11}$  mode of the dielectric rod.

The multi-channel spark gap of the LIA must switch the current determined by the PFLs charging voltage and wave impedance, that is about 100 kA in our case. The current division into channels allows avoiding the erosion of the spark gap electrodes in the repetitive operation mode. Assuming the limit for commutated charge in one channel is  $\sim 10^{-3}$  C, one can conclude that twelve channels would provide stable spark gap operation without blowing. The multi-channel spark gap is fixed at the end flange of LIA tank, and spark develops with the toroidal dielectric chamber as seen in Fig.29. More detailed design of the multi-channel spark gap is shown schematically in Fig.31.

Between the solid electrodes 1, 2 connected to the PFLs, the electrodes 4 are located, which are the anodes of spark gap channels. They are surrounded by the ferrite cores 5 with the common short-circuited winding 6 made as two parallel turns to reduce the inductance.



The triggering electrodes 3 are inserted into the spark space. The synchronization of channels is provided both by forced current division (if some gap is broken down, its current is limited by remagnetization current of the core 5, and the voltage is induced that charges additionally the gaps still not initiated) and by controlling the discharge, like in spark gaps with field distortion, adjusting elements of triggering circuit.

Fig.31. Schematic of the multi-channel spark gap.  
1 – potential electrode, 2 – grounded electrode,

3 – triggering electrodes, 4 – channel anodes,  
5 – ferrite cores, 6 – common short-circuited winding, P – triggering spark gap, PTR – pulsed transformer.

The LIA pulsed transformer PTR charges the capacity of the PFLs and forms the current to demagnetize the cores of the induction system. The triggering spark gap P is launched by an external generator that allows one to synchronize the LIA with an external source of the microwave drive signal. Let us consider the problem of synchronization in a bit more detail.

It is assumed that in the future proof-of-principle experiments, a microwave pulse compressor will be employed to produce an antenna feed and amplifier RF drive signal in order to have its pulse length less than a beam one. Hence, the entire experimental installation includes five systems to be triggered and contains (i) switch to turn on guiding magnetic field, (ii) switch of LIA primary storage charging the PFLs, (iii) switch that triggers an X-band pulsed magnetron oscillator pumping the microwave storage cavity, (iv) LIA triggering spark gap P mentioned above, and (v) spark gap that triggers the microwave pulse compressor. This is illustrated in Fig.32.

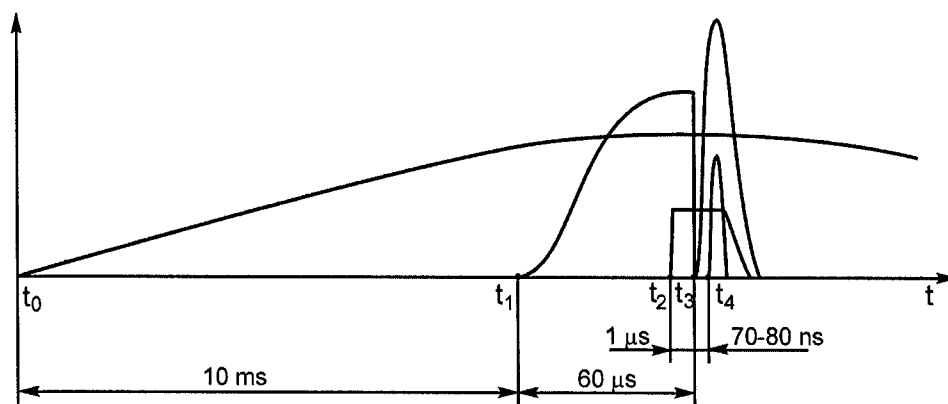


Fig.32. Time scale and moments of launching magnetic field solenoid ( $t_0$ ), LIA pulsed transformer charging the PFLs ( $t_1$ ), pulsed magnetron ( $t_2$ ), LIA triggering spark gap ( $t_3$ ), and microwave pulse compressor spark gap ( $t_4$ ).

The synchronization is realized as shown in the functional diagram in Fig.33. The installation is launched by means of the delayed-pulse oscillator, which forms two output pulses: one for discharging the capacitors battery, the power supply for the guiding magnetic field solenoid, and another one, delayed by  $\sim 10$  ms (for the battery we used), for activating the LIA control system. As a result, the accelerator is fired at the maximum value of the guiding field. In its turn, the LIA control system forms three output pulses. The first pulse

activates the thyristor switch of the LIA power supply circuit, so that the LIA primary storage discharges through the winding of pulsed transformer, and the PFLs are charged. The time of PFLs charging is  $\sim 60 \mu\text{s}$ , and the typical time of storing microwave energy in the pulse compressor cavity is  $\sim 1 \mu\text{s}$ . Hence, the second pulse produced by the LIA control system is formed with  $59 \mu\text{s}$  delay and launches the X-band pulsed magnetron. Then, after  $1 \mu\text{s}$  delay, the LIA control system generates the third pulse. This pulse serves for activating both the LIA and microwave pulse compressor triggering spark gaps. The synchronization between the electron beam and microwave drive pulses is achieved using a cable delay line of proper length.

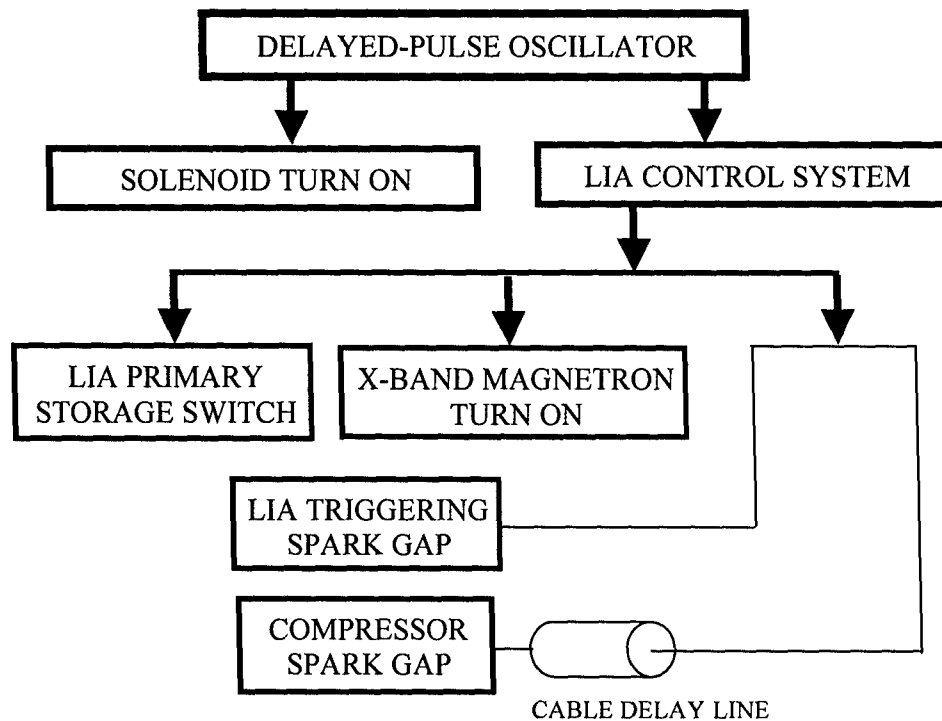


Fig.33. Functional diagram of the antenna-amplifier synchronization.

In order to estimate the required delay of the cable, one needs to take into account, on the one hand, the actuation delays of the LIA triggering and multi-channel spark gaps and the length of the PFLs and, on the other hand, the actuation delay of the compressor spark gap and the length of the microwave transmission system from the compressor output to the LIA cathode. Finally, the moment of microwave drive pulse entering the interaction space should fall to around the middle of the LIA voltage pulse. All this results in 70-80 ns estimated delay,

i.e., reasonable cable length (it is to be adjusted for real experiments on gain demonstration). Typically, the LIA jitter is several nanoseconds (it is determined by the operation of multi-channel spark gap), and typical jitter of an X-band pulse compressor is also  $\leq 10 \text{ ns}$  [16]; therefore one can expect reliable synchronization of these systems.

The power supply circuit for the LIA module is presented in Fig.34. It consists of the capacitive storage, primary switch, and the pulsed transformer. In the circuit of storage charging, the charging choke, ac

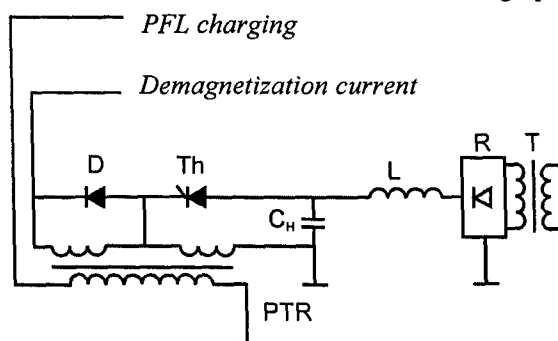
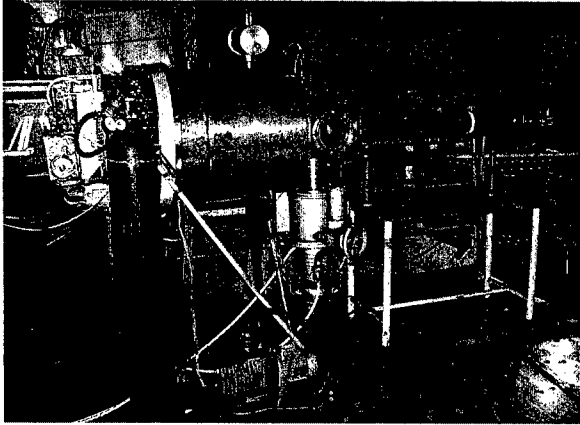


Fig.34. LIA power supply circuit. T – ac main transformer, R – rectifier, L – charging inductance,  $C_H$  – primary storage, Th – thyristor switch, D – diode. PTR – pulsed transformer.

transformer, and rectifier are used. For the repetition rate of 50 pps, the estimated main power consumption for the LIA module turns out to be  $\sim 2.5$  kW. As the power consumption is not high, the power supply circuit can be compactly placed on the insulated plate fixed by studs at the butt-end of the module.



The LIA module is shown in Fig.35 along with the available long solenoid employed for the model experiments on beam transport (a much shorter solenoid is planned to be used in the future proof-of-principle experiments with the microwave drive signal). The dimensions of the module itself (with the power supply seen at the left) are  $\sim 70$  cm diameter and  $\sim 120$  cm length.

Fig.35. Appearance of the LIA module and setup used in model experiments on beam transport.

#### b) Annular beam generation and transport with a dielectric inside

The experiments on beam generation and transport by the guiding magnetic field with the dielectric rod inside in the absence of an external microwave signal are, as was mentioned above, the key model experiments. Their goal is to study plasma formation at the dielectric surface and estimate how dense this plasma is. If the density, by its order of magnitude, does not exceed  $10^{12} \text{ cm}^{-3}$  (that means the plasma frequency is less than the operating frequency of the X-band), the presence of plasma does not significantly affect the electrodynamic properties of the system, so that the concept of antenna-amplifiers can be realized with a dielectric rod antenna.

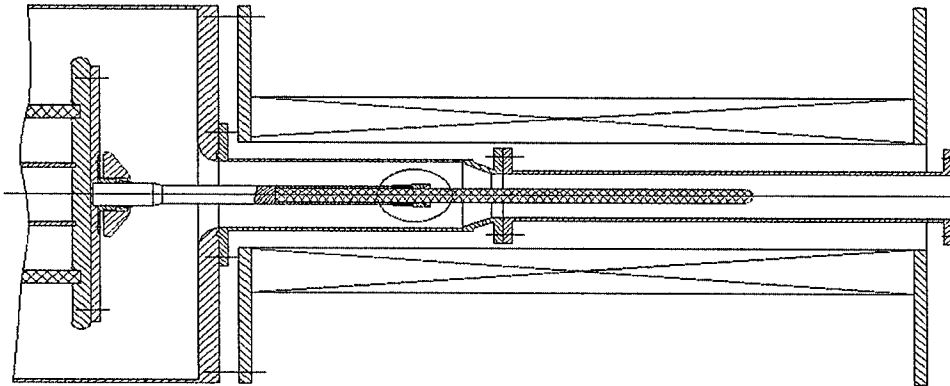
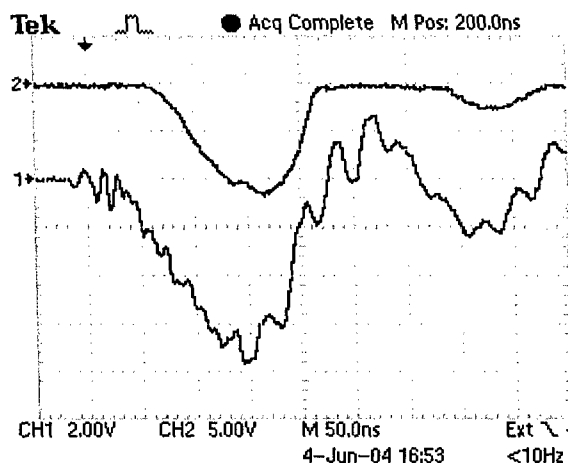


Fig.36. Schematic of experimental geometry. Circle marks the cathode of magnetically insulated coaxial diode.

Detailed geometry of the experiments is presented in Fig.36. It includes the LIA vacuum chamber with its insulator, high-voltage flange, and cathode holder (shown schematically in Fig.29), the coaxial magnetically insulated diode (60 mm anode and 20 mm cathode edge diameters), the tapered buffer section (26 mm length), and the drift tube (40 mm diameter). One can see the cathode holder alignment unit at the high-voltage flange; the magnetic field axis was aligned by means of adjusting bolted joints between the solenoid flange and the vacuum chamber. The cathode edge is located in the region of uniform magnetic field (52 mm from the drift tube entrance). Dielectric rods (12 mm diameter) were inserted through the

hollow cathode into the hollow end section of cathode holder as a tight fit. Rods of different length were used in experiments; the maximum was 240 mm from the cathode edge to rod end. Three different materials were employed for rods: plexiglas, polyethylene, and quartz.

The LIA accelerating voltage was measured by the capacitive voltage divider located at the inner surface of the vacuum chamber cylindrical wall. The Rogovsky coil was placed around the vacuum chamber to measure the LIA current. The electron beam current in the drift tube was measured by the Faraday cup movable along the tube. The means of plasma diagnostics will be discussed below. The magnetic field in all shots made in the main course of experiments was as high as 2.6 T. The typical LIA voltage and beam current pulses are shown in Fig.37. One can see that the values of voltage and current, together with the



geometrical parameters, form the set of parameters corresponding to the mentioned Set 1 that was chosen for initial experiments. The only exception is the dielectric constant of rod material; we just tested available materials, and the proper choice of material for the rod to be employed in the real antenna-amplifier device is a separate task, which is discussed a little below, but rather not duly considered here.

Fig.37. Oscilloscope traces of accelerating voltage (channel 1, ~70 kV/div.) and electron beam current (channel 2, ~450 A/div.) pulses.

The plasma could be produced either due to placing the rod inside the cathode under high voltage that causes the surface breakdown, or as a result of some processes occurring during beam propagation along the rod. First, we have studied the possibility of plasma formation inside the cathode. The details of the initial cathode design are shown in Fig.38. It is seen that the triple point circle, where the rod contacts the cathode inner surface, is rather close to the cathode edge, where high voltage is applied. This resulted in a very dense plasma production, as one can see from the image also presented in Fig.38. There are two concentric circles of, in fact, the same brightness; one corresponds to the cathode edge diameter, and another one corresponds to the rod diameter. Similar images were obtained with long, extending into the drift tube, and short, just slightly sticking out of cathode, plexiglas rods at the given witness plate position. This proves that the inner trace is originated from inside the cathode. The same brightness means that the plasma density at the triple point region is as high as the density of plasma formed at the cathode edge due to explosions of micro-protrusions on metal surface. Such plasma would certainly prevent RF fields of an X-band drive signal from coupling to the electron beam outside the rod; this is not acceptable.

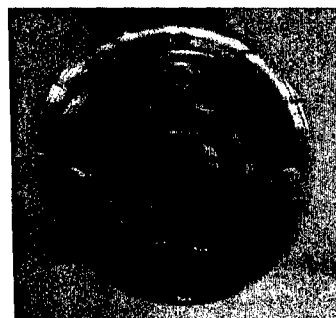
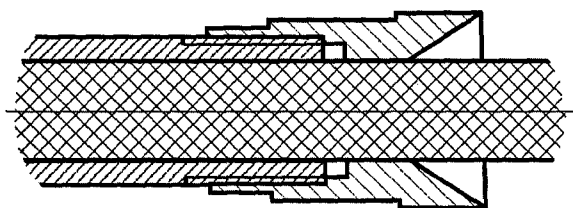


Fig.38. Initial cathode design (left) and image produced with this cathode on the witness plate downstream of the

short (25 mm from the cathode edge to rod end) plexiglas rod (right).

Then the cathode design was modified as shown in Fig.39 in order to "hide" the triple points inside, much farther from the cathode edge. As a result, plasma production from this place has been eliminated. The image obtained on the copper foil in case of the short rod inserted into the modified cathode shown in Fig.39 is the same as one produced by the electron beam without dielectric at all.

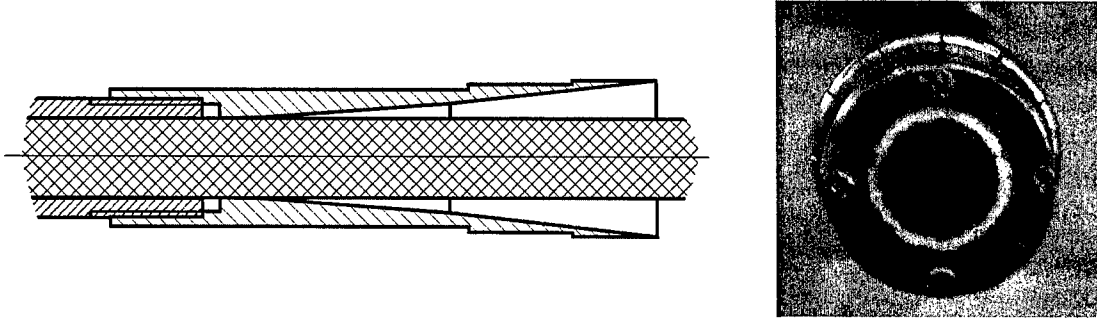
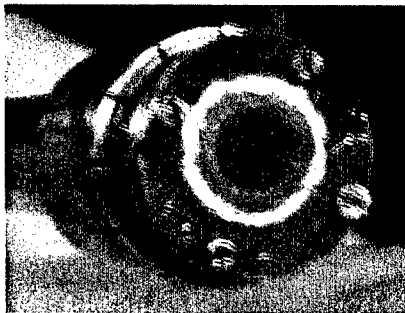


Fig.39. Modified cathode design (left) and image produced with this cathode on the witness plate downstream of the short (12 mm from the cathode edge to rod end) plexiglas rod (right).

However, the trace on the witness plate inside the trace produced by the main beam appeared in case of the long dielectric rod extended into the drift tube. The corresponding image obtained for the maximum rod length is presented in Fig.40. It is seen that the inner trace is less bright than the main beam trace, in difference of Fig.38, i.e., the plasma produced at the rod surface is not so dense. As the inner trace appeared only when the rod extended into



the drift tube, one can conclude that the critical place for plasma formation at the rod surface is at the tapered buffer region. After many shots done, we got another evidence for that: the traces of surface breakdown appeared on the rod namely at the location of tapered region. This was observed for all rod materials tested.

Fig.40. The same as in Fig.39 for the long rod (240 mm from the cathode edge to rod end).

The main course of the experimental work was aimed at obtaining data concerning the actual density of plasma produced at the dielectric rod surface. Its direct measurements with the use of Langmuir probes that were planned initially have turned out impossible. In test shots made with the Faraday cup moved right up to the end of plexiglas rod, short-circuiting was observed. That means that the surface discharge develops along the dielectric towards, in fact, a grounded electrode at the rod end. Hence, placing a Langmuir probe at the rod surface would cause such discharge, i.e., formation of another, "artificial" plasma, which is irrelevant to the physical situation of beam generation and transport with a dielectric inside. This is because the dielectric contacts the cathode under high voltage, unlike the situation in conventional dielectric Cherenkov masers [5], where the beam propagates inside a dielectric liner adjoining a conducting tube at ground potential.

Therefore, the main diagnostic means implemented for estimations of the plasma density was based on measuring the current transferred by the inside of annular beam, which produces this less bright trace on the witness plate seen in Fig.40. We assume that the source of this current is the plasma at the rod surface; hence, considering it as the electron saturation current, one can estimate the near-surface plasma electron density  $n$  from the formula



$j \approx nev_T$ , where  $j$  is the measured current density and  $v_T$  is the thermal velocity. Let us next assume that the electron plasma temperature is a few eV (this is typical for surface discharge plasma); then, one can calculate the electron saturation current for the characteristic plasma density of  $10^{12} \text{ cm}^{-3}$  mentioned above and obtain  $j \sim 20 \text{ A/cm}^2$ . It remains to measure the current through some known area and compare the current density to this figure.

We have used the special composite Faraday cup with two collectors capable of measuring both the main electron beam current and the current transferred inside the beam. The design of this Faraday cup is shown in Fig.41. The main beam current is delivered to the outer collector 1. The inner collector 2 is made changeable, so that its diameter could be varied; maximum diameter was anyway less than the inner diameter of the beam. The added pieces to the outer collector and the foil diaphragm 5 protected the insulator 4 of inner collector from the plasma produced by the beam. On the other hand, using diaphragms with different diameters of the hole allowed for obtaining a dependence of the current delivered to the inner collector on the hole size, so that one could get an idea about the plasma density

radial profile. Also, the diaphragms served as witness plates showing the degree of beam-rod alignment. The collet 6 provides a contact with the drift tube wall, and registration cables go outside through the hollow supporting stick 7.

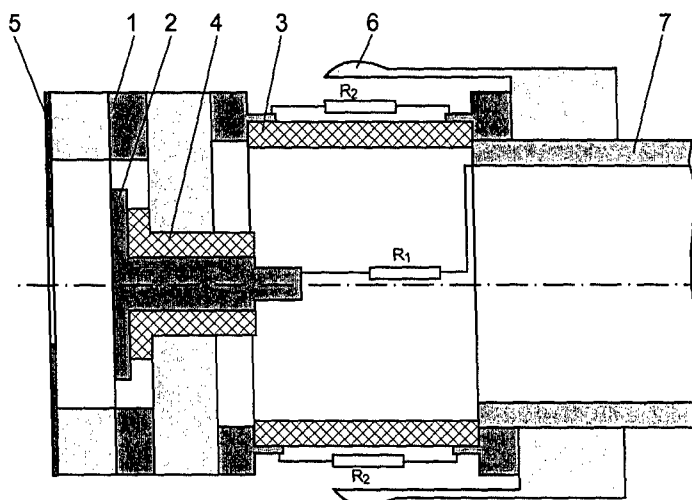


Fig.41. Schematic of the composite Faraday cup. 1 – outer collector, 2 – inner collector, 3 – insulator of outer collector, 4 – insulator of inner collector, 5 – diaphragm (witness plate), 6 – collet, 7 – grounded stick (support).

An example of current pulses registered by this Faraday cup is presented in Fig.42. In this case (and for all oscilloscope traces presented below), the rod of maximum length was installed, 240 mm counting from the cathode edge. One can see that the current delivered to the inner collector is  $\sim 30 \text{ A}$  here, for 15.4 mm diameter of the diaphragm hole. A rough assumption now would be to estimate current density taking the area of annulus between the diaphragm hole and rod cross-section. This gives  $j \sim 40 \text{ A/cm}^2$ . However, there is also a contribution from the central region to the current delivered to the inner collector. It is caused by some emission from the rod end – we checked this by means of using the diaphragm with a small diameter of the hole. In this case, we sometimes observed small signals with the solid rod, but with the rod made annular at the end region, these signals totally disappeared.

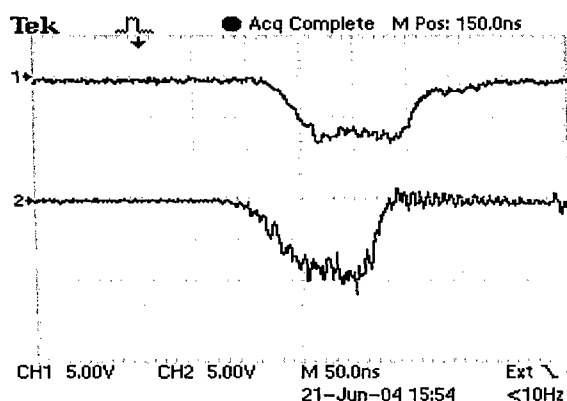


Fig.42. Current pulses delivered to inner (channel 1,  $\sim 21 \text{ A/div.}$ ) and outer (channel 2,  $\sim 450 \text{ A/div.}$ ) collectors of the composite Faraday cup placed 52 mm downstream of the plexiglas rod end. The diaphragm hole is of 15.4 mm diameter.

Therefore, more correct approach consists in obtaining data with different diameters of the diaphragm hole; the difference in the data obtained with the greater and smaller holes gives, statistically, the current transferred through the annulus representing the area difference. We have carried out these studies. It should be noted here that shot-to-shot stability of the current pulses at the inner collector (and, hence, plasma density) in the reported experiments was not very good. Oscilloscope traces obtained in the series of consecutive LIA shots giving an example for that are shown in Fig.43. In this example, the rod material is polyethylene.

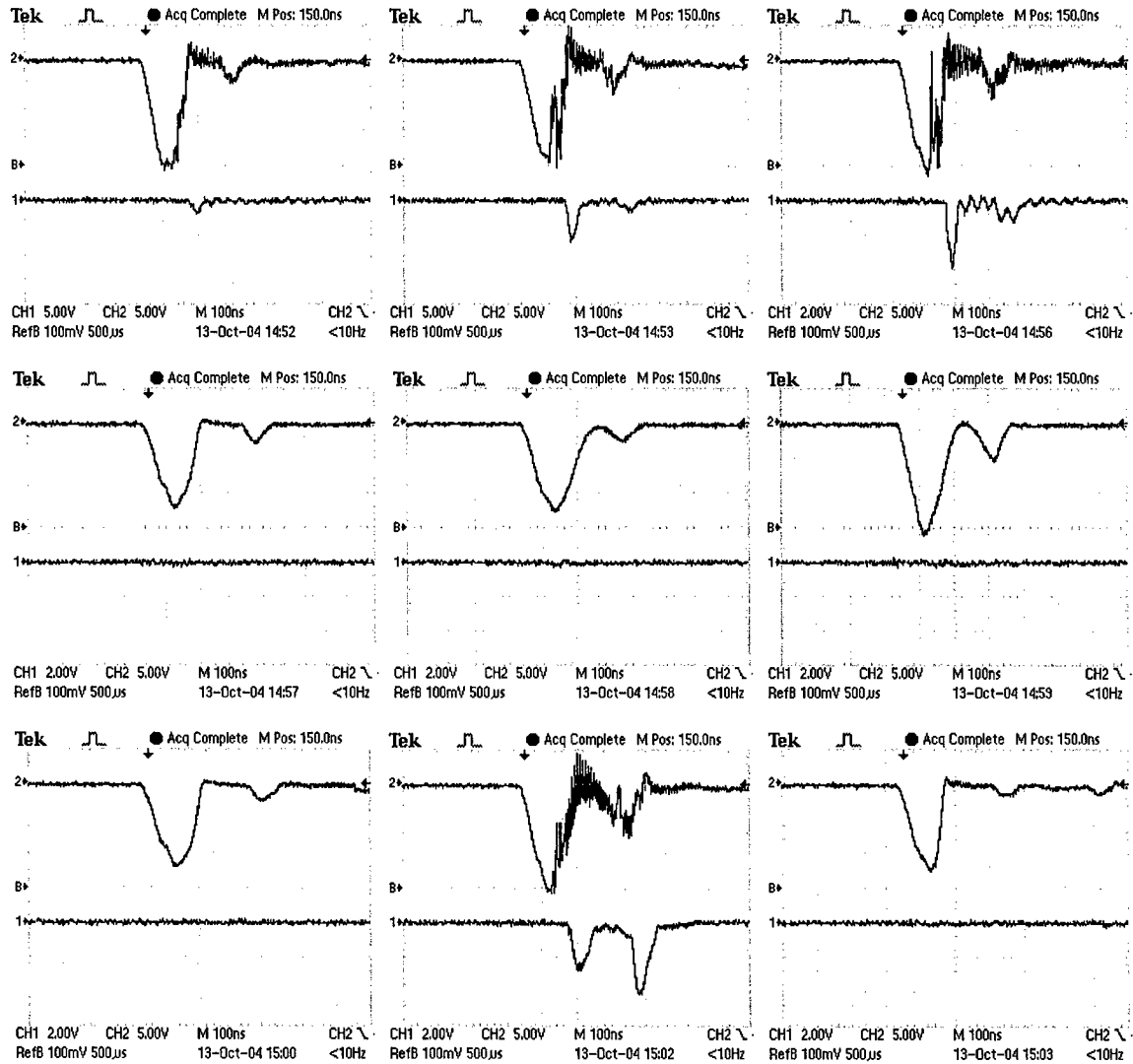


Fig.43. Current at inner (channel 1, ~110 A/div. in two first plots, ~44 A/div. in other plots) and outer (channel 2, ~450 A/div.) collectors in 9 consecutive LIA shots. Polyethylene rod, 12 mm diameter of the diaphragm hole.

It is seen that in this series, there are "good" and "bad" pulses; the quality is determined by the magnitude of signal recorded in channel 1, which is associated with acceptably low or too high plasma density. The difference in pulse amplitudes could reach orders of magnitude. The interference seen in traces of main beam current pulses (channel 2) in "bad" shots is caused right by the influence of a large signal in channel 1 on the registration circuit. Depending on the degree of beam-rod alignment and the level of vacuum in the system, "bad"

pulses appeared either more or less frequently. In Fig.43, a medium example is presented. One can conclude from this series that "bad" pulses may appear due to desorption occurred during first shots, and then, after pumping desorbed gas out, they disappear. However, we did not get a reliable confirmation of this assumption. Additional examples of consecutive LIA shots series can be seen in Figs.44-46. In any case, with the vacuum level ( $\sim 7 \cdot 10^{-5}$  torr) accessible in our experiments, "bad" pulses have not been eliminated absolutely. Let us note also that we did not get convincing evidences of the rod material influence on discussed shot-to-shot stability.

In Figs.44-46, the oscilloscope traces are shown that were recorded in shots made with the quartz rod and varied diameter of the diaphragm hole (12, 13, and 14 mm, respectively). This is the example of data used for the estimation of the near-surface plasma density. In spite of the presence of some "bad" pulses, one can see from the plots that the current delivered to the inner collector of the composite Faraday cup on average increases with increasing diameter of the hole.

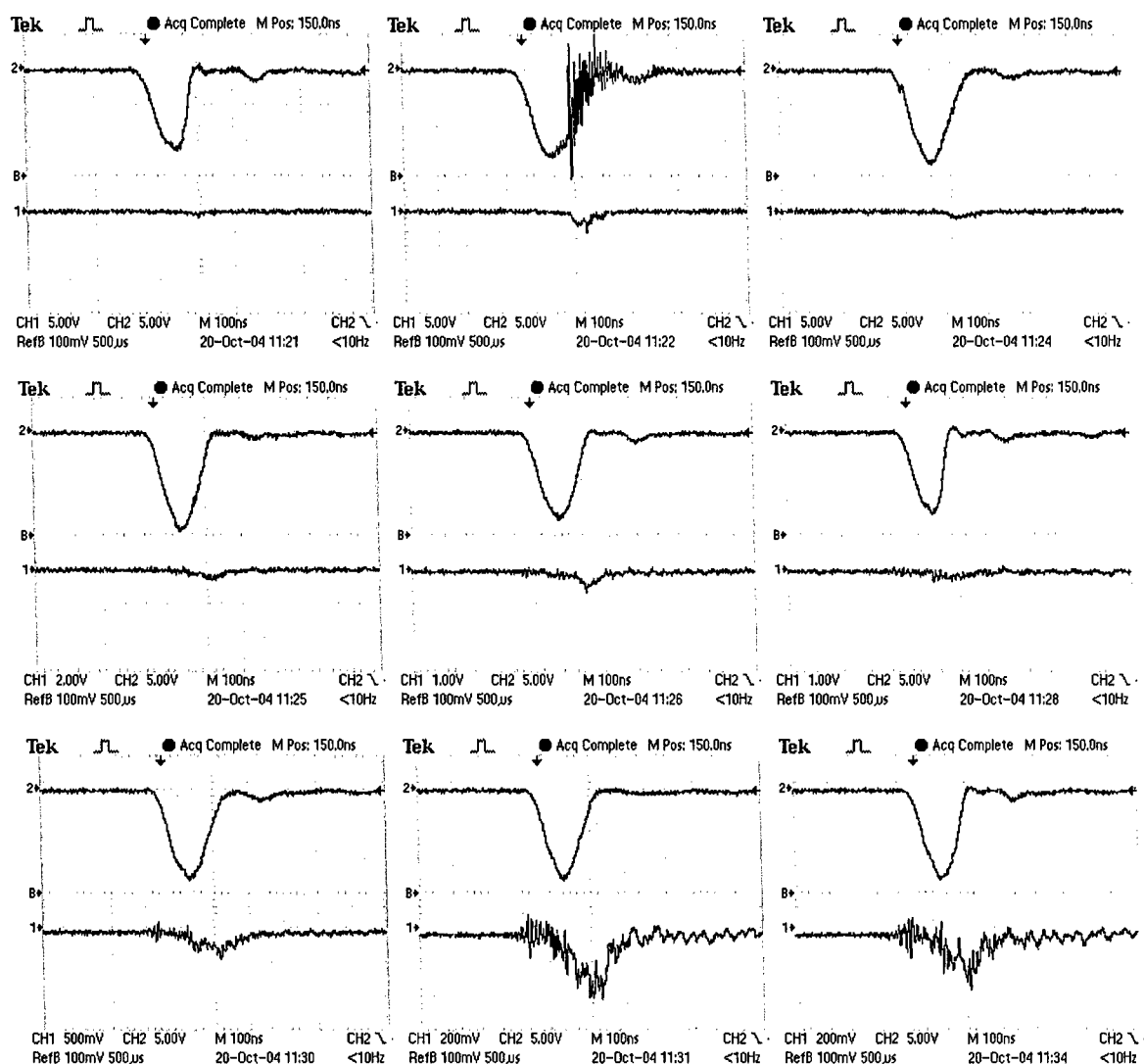


Fig.44. The same as in Fig.43 for the quartz rod and  $\varnothing 12$  mm diaphragm hole. The current scales for the records in channel 1 are as follows. Top plots –  $\sim 110$  A/div. Middle plots: left –  $\sim 44$  A/div.; others –  $\sim 22$  A/div. Bottom plots: left –  $\sim 11$  A/div.; others –  $\sim 4.4$  A/div.

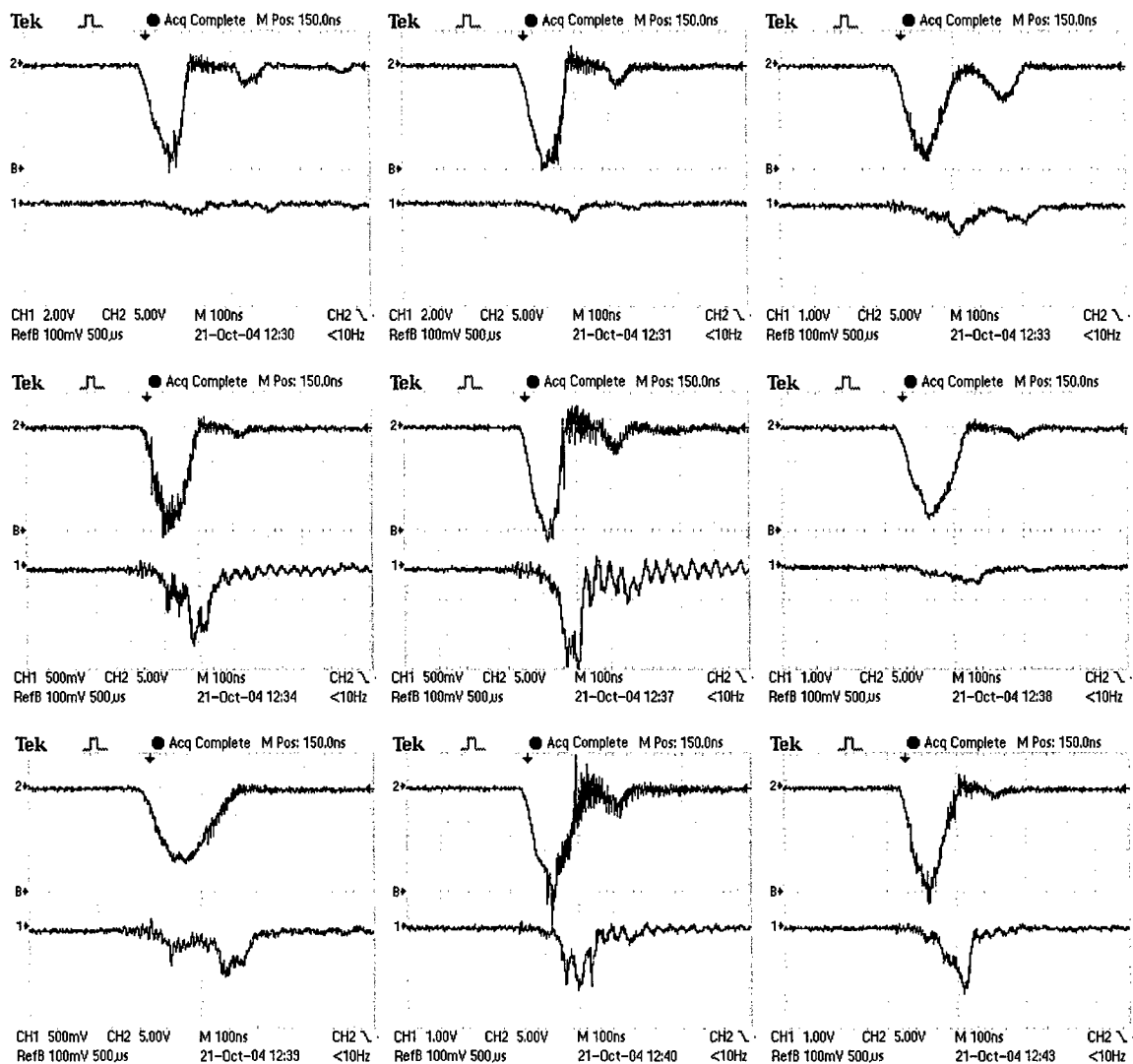


Fig.45. The same as in Fig.43 for the quartz rod and Ø13 mm diaphragm hole. The current scales for the records in channel 1 are as follows. Top plots: right – ~22 A/div.; others – ~44 A/div. Middle plots: right – ~22 A/div.; others – ~11 A/div. Bottom plots: left – ~11 A/div.; others – ~22 A/div.

Statistical treatment of such data yields finally the estimation for current density (within the range of radial coordinate from 6 to 7.5 mm)  $j \sim 20 \div 30 \text{ A/cm}^2$ . Although accuracy of our measurements is not quite satisfactory, one can, nevertheless conclude that, by the order of magnitude, the density of the near-surface plasma is  $\sim 10^{12} \text{ cm}^{-3}$ . This can be considered more or less acceptable for the X-band antenna-amplifier operation; nevertheless, investigations are needed to find the conditions (beam-rod alignment, vacuum level, processing of the rod surface, maybe, rod material), at which the plasma density is reduced more, and the reproducibility is better. Also, since it has been found that the critical place for plasma formation at the rod surface is at the tapered buffer region between the diode and narrower drift tube, a solution could be in using quasi-planar diode geometry instead of the coaxial one, so that the buffer section is absent. MAGIC simulations for such geometry have been performed (see Fig.22). In this case, though, a larger solenoid is required to magnetize the region of beam formation.

At last, let us briefly discuss the problem of material choice for the dielectric rod antenna on the basis of comparison of the three materials that we tested. As was said above, regardless

of the material, the rod surface breakdown occurs at the axial location of tapered section. In the course of experiments, it has been observed that after many shots, the plexiglas and polyethylene rods exhibit also traces of surface breakdown along all their length from the buffer section to the rod end. In any case, breakdown traces at the tapered region appeared first, and the region between the cathode and tapered section remained clean. For the quartz rod, breakdown traces in the drift tube region were not observed.

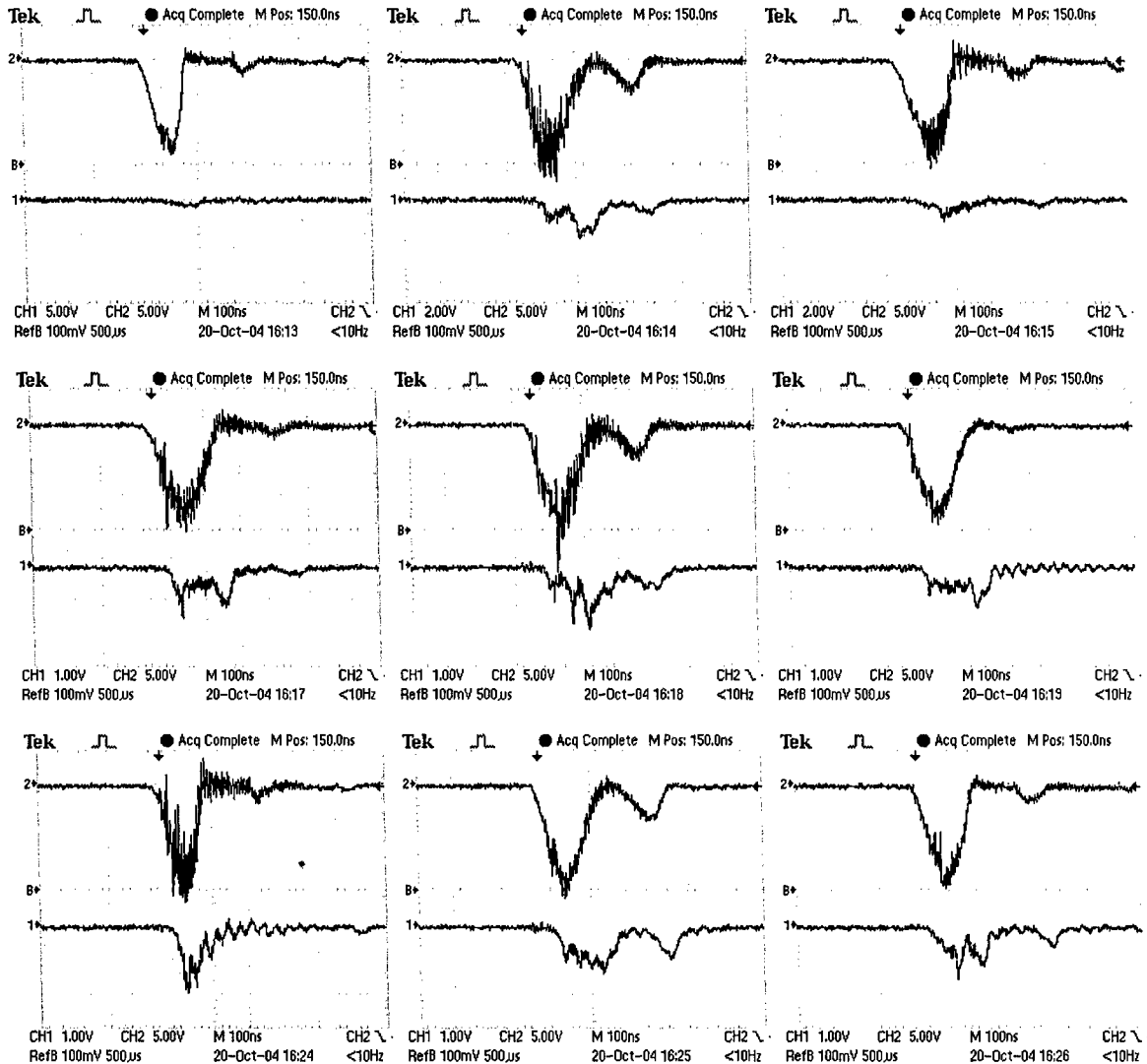


Fig.46. The same as in Fig.43 for the quartz rod and  $\varnothing 14$  mm diaphragm hole. The current scales in channel 1 are as follows. Top plots: left –  $\sim 110$  A/div.; others –  $\sim 44$  A/div. Middle and bottom plots –  $\sim 22$  A/div.

Photos of the three rods that operated in the experiments are presented in Fig.47. An important thing is seen from the top picture – for the plexiglas rod, with which the greatest number of shots was made, a small "waist" (0.3 mm reduction of rod diameter under the cathode edge) has been observed. It is caused, most likely, by the UV radiation from the cathode plasma heating the rod up to material transfer off, since plexiglas softening point is as low as  $90^{\circ}\text{C}$ . Evidently, plastic rods are rather not appropriate for an operating device, and materials with high softening (melting) temperature like quartz or titanium silicate glasses should be employed.

Finally, the experiments performed allow us to conclude that the concept of antenna-amplifier based on a dielectric rod antenna can be considered realizable.

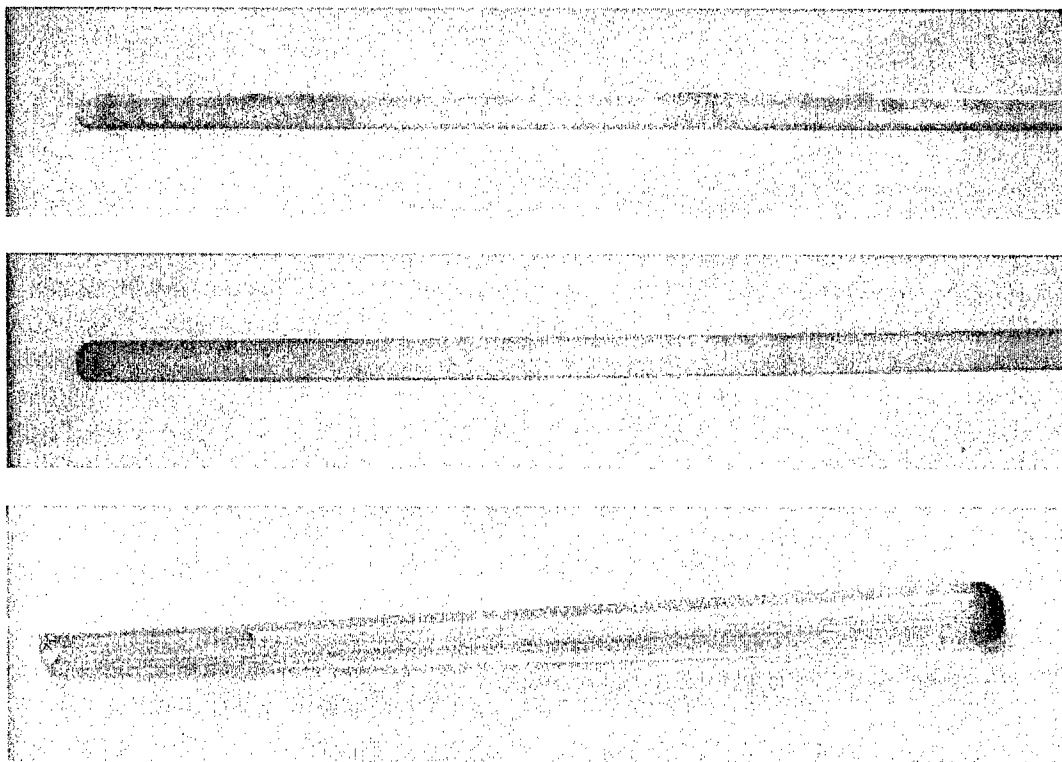


Fig.47. Pictures of dielectric rods after experiments: plexiglas (top), polyethylene (middle), and quartz (bottom).

### c) Microwave transmission and antenna pattern measurements

Studies of microwave transmission and antenna pattern without electron beam generation have been carried out using the low-power ( $\sim 0.1$  W) frequency tunable cw X-band oscillator. The measurements have been made in different conditions: (i) with a standard rectangular waveguide as a feed waveguide, (ii) with the microwave transmission system specially designed so that a circular antenna feed waveguide could serve as a LIA cathode holder, and (iii) with the above system incorporated into the LIA chamber assembled with the electron diode and drift tube used in experiments on beam transport, i.e., in the actual geometry of antenna-amplifier device (except for a vacuum window presence).

The main goal of these experiments was to make clear how the actual geometry affects the antenna efficiency, i.e. the level of reflections and directivity, along with the far field radiation pattern. Also, we pursued the objective of checking in principle known features of dielectric rod antennas [7] with our prototype samples, so that we studied how antenna characteristics depend on the rod length and diameter, radiation frequency, and kind of feed waveguide.

Prototype antennas were made of polyethylene (as available material at the moment). Its dielectric constant was measured in the X-band using the standard waveguide slotted line-based technique; the result was  $\epsilon \approx 2.26$ . The diameter of the rod was chosen from the consideration of providing proper calculated phase velocities of the  $HE_{11}$  mode in the frequency range given by the employed oscillator (we tested rods of 16 and 15 mm diameter with the rectangular feed waveguide and rods of 15 mm diameter with the circular feed waveguide). The antennas of two different lengths (17 and 25 cm) were tested. They were made with no tapering, just with rounded ends.

The works on microwave transmission system development and antenna studies included the following stages:

1. Measurements of characteristics of sample antennas fed through the standard X-band rectangular waveguide (23×10 mm, fundamental  $TE_{10}$  mode) in the unechoic chamber.
2. Design and fabrication of the microwave transmission system for antenna feeding through the circular waveguide in its fundamental  $TE_{11}$  mode, so that the feed waveguide with a horn could play the role of LIA cathode holder with a knife-edge cathode of electron diode.
3. Studies of the fabricated system and sample antennas fed through the circular waveguide in the unechoic chamber.
4. Studies of the system incorporated into the LIA chamber with the anode of electron diode and drift tube (as in experiments on beam transport); in this case, antennas radiated into the free space.

Schematic of the measurements in the unechoic chamber is shown in Fig.48. The dimensions of the unechoic chamber are  $\sim 120 \times 120 \times 350$  cm, so that the location of the receiving horn was well in the far field zone of tested antennas. The receiving horn was fixed, whereas the radiating antenna could be rotated both in the horizontal and vertical planes. In this configuration, the inaccuracies of measuring the angle of antenna turning  $\varphi$  and the distance between the radiating and receiving antennas  $R$  lead to the inaccuracies in the antenna pattern angular width, which can be estimated as  $\sim \arctan(l \sin \varphi / R) / \varphi$  and  $\sim 2l(1 - \cos \varphi) / R$ , respectively, where  $l$  is the length of the rod antenna. For angles of antenna rotation  $\varphi \leq 20^\circ$ , this gives the summed inaccuracy not exceeding 15%.

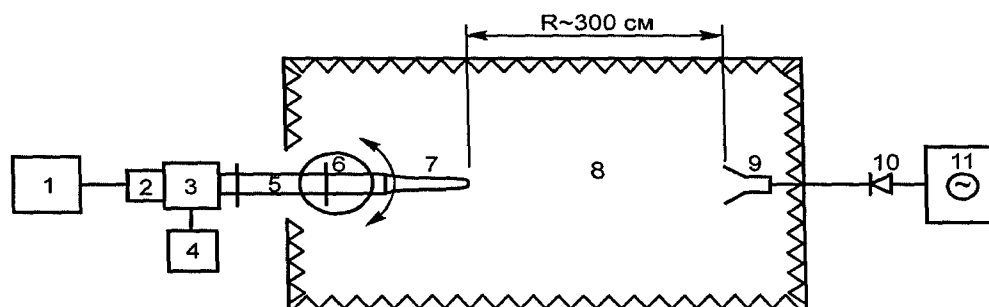


Fig.48. Experimental setup used for antenna pattern measurements in the unechoic chamber. 1 – low-power cw X-band oscillator; 2 – coax-waveguide transformer; 3 – microwave circulator; 4 – matched load; 5 – feed waveguide; 6 – tripod with the mechanism providing rotational displacement; 7 – rod antenna; 8 – unechoic chamber; 9 – receiving horn antenna; 10 – calibrated detecting unit; 11 – oscilloscope.

The antenna patterns we obtained with the use of the rectangular feed waveguide practically do not differ from those we got later with the circular feed waveguide concerning their frequency dependence and the dependence on the rod length, the results presented below. With the rectangular feed waveguide, we compared the rods of two different diameters. It turned out, as expected, that for the thicker rod, a significant level of side lobes appeared at a lower frequency than for the thinner one. With the circular feed waveguide, we tested only rods of one diameter.

The design of the microwave transmission system was already briefly described above in the section a). In Fig.49, it is shown again, together with the dielectric rod. The input X-band signal goes through the standard rectangular waveguide in its  $TE_{10}$  mode; then it enters into the rectangular-to-circular waveguide transformer. The end cross-section of the transformer is of 23 mm diameter, so that the only lowest  $TE_{11}$  mode of a circular waveguide is supported within the frequency range of the employed oscillator. This transformer was designed as a transformer of minimum length providing the reflection coefficient  $\Gamma^2 < 0.005$  for the

frequency range from 8.7 to 9.7 GHz on the basis of known expressions giving the axial profile of wave impedance [17]. Next to this transformer is the matching section between the circular waveguides of 23 and 16 mm diameters. For an empty waveguide of 16 mm diameter, the operating frequencies are already below cutoff, so that the signal propagation is provided due to filling with dielectric, and matching is achieved by tapering the input part of the rod as well as the conducting wall. Finally, the dielectric-filled waveguide of 16 mm diameter ends with the cathode serving as the horn of 20 mm aperture diameter, which excites the operating  $HE_{11}$  mode of the rod antenna. The rod is made sectional (in difference of the experiments on beam transport) in order to provide its needed extension out of the horn.

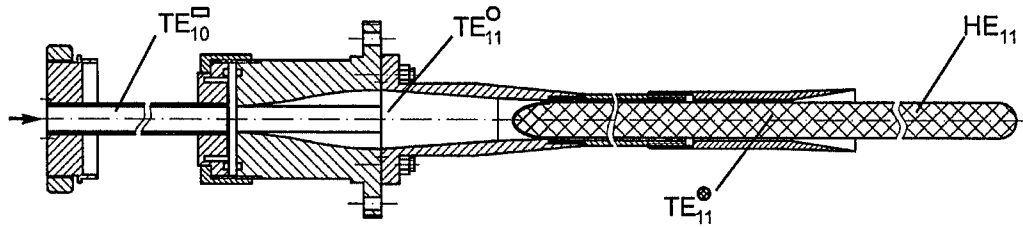


Fig.49. The microwave transmission system (schematic).

Some results of the measurements of the antenna pattern performed with this designed and fabricated system in the unechoic chamber are shown in Fig.50. The values of antenna length  $l$  given on these plots correspond to the length of rod extension out of the horn aperture. One can see that the obtained values of the main lobe angular width are of the same order as those known for dielectric rod antennas [7]. The longer antenna has a higher directivity as expected ( $\sim 15-17^\circ$  FWHM width), however, it exhibits much faster growth of the side lobes level with increasing frequency. Let us note here that suppression of the side lobes by proper tapering of the antenna radius was not our goal; this problem can be solved using methods of antenna synthesis regardless of issues connected with an antenna-amplifier device operation.

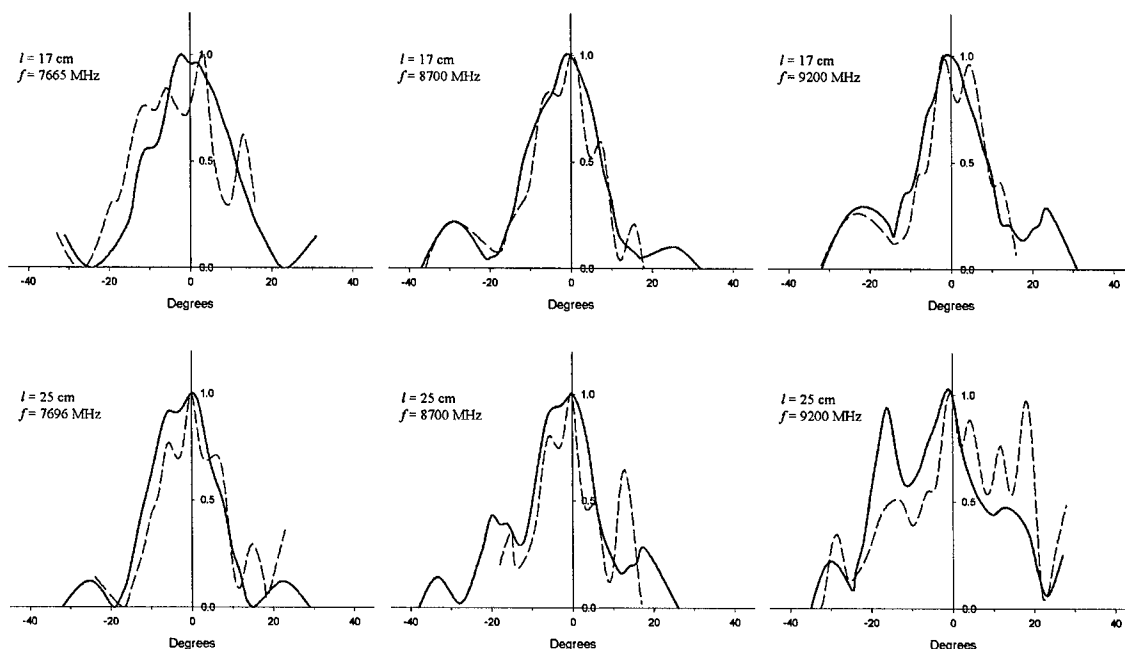


Fig.50. Power delivered to the receiving antenna (a.u.) vs. angle of rod antenna rotation in the H-plane (solid curves) and E-plane (dashed curves) at different frequencies for two different antenna lengths (measured in the unechoic chamber).



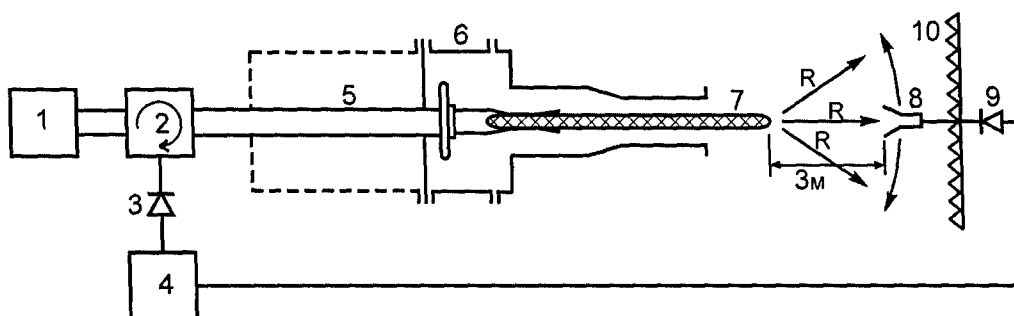
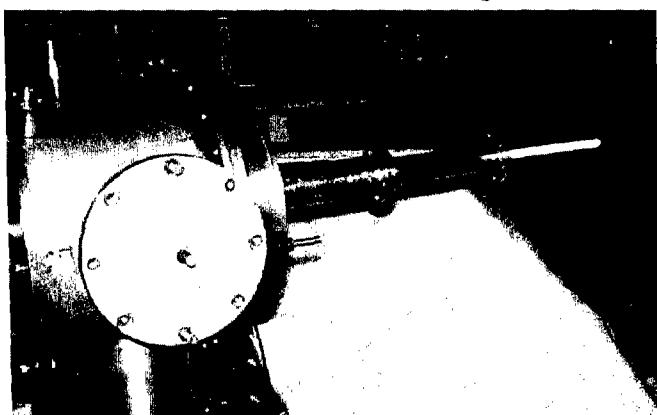


Fig.51. Experimental setup used for radiation pattern measurements in the free space (system is inside the LIA). 1 – low-power cw X-band oscillator; 2 – waveguide circulator; 3 – detecting unit for reflected signal registration; 4 – oscilloscope; 5 – microwave transmission system; 6 – LIA chamber; 7 – rod antenna; 8 – receiving horn antenna; 9 – detecting unit; 10 – microwave absorber.

Schematic of the experiments with the microwave transmission system incorporated into the real hardware of LIA chamber, anode, and drift tube is presented in Fig.51. In these experiments, it was the receiving antenna that was displaced in the far field zone along the arc of circle of 3 m radius in the horizontal plane. The system radiated into the free space as shown in the figure. The whole system including radiating antenna was fixed; in order to obtain radiation patterns in H- and E-planes, we rotated it around its own axis by  $90^\circ$ , so that the plane of receiving antenna displacement became either H- or E-plane depending on the orientation of the rectangular waveguide of the system. As is seen from Fig.51, the reflected signal existing in the actual geometry of the antenna-amplifier was registered as well as the signal delivered to the receiving horn.

The appearance of LIA chamber, anode and drift tube with the radiating antenna can be seen in Fig.52. It should be emphasized that the entire length of the polyethylene rod in these experiments was  $\sim 30$  cm greater compared to the case of isolated antenna. However, we tested, in fact, antennas of the same lengths: in case of actual antenna-amplifier geometry, the



length is defined by the rod extension out of the drift tube end flange, whereas for isolated antennas, it is the distance between the rod end and feed horn aperture (cathode edge).

Fig.52. External view of the rod antenna fed by the developed microwave transmission system incorporated into the hardware of model experiments on electron beam transport.

Thus we were able to achieve the goal of determining purely the influence of real geometry surrounding the dielectric rod on the antenna characteristics. The results of the radiation pattern measurements for the same frequencies and antenna lengths as shown above in Fig.50 are presented in Fig.53. Comparing the two figures, one can see that the obtained data demonstrate very similar features, i.e., the real geometry of the device practically does not change the angular distribution of radiated power and its dependence on frequency in comparison with those of the isolated antenna. The main lobe angular width vs. frequency dependence measured in the real geometry for the two antenna samples is shown in Fig.54.

As is seen, for the longer antenna, the main lobe is narrower, but smeared at lower frequencies, so that there are no data to be plotted at frequencies exceeding 8.9 GHz.

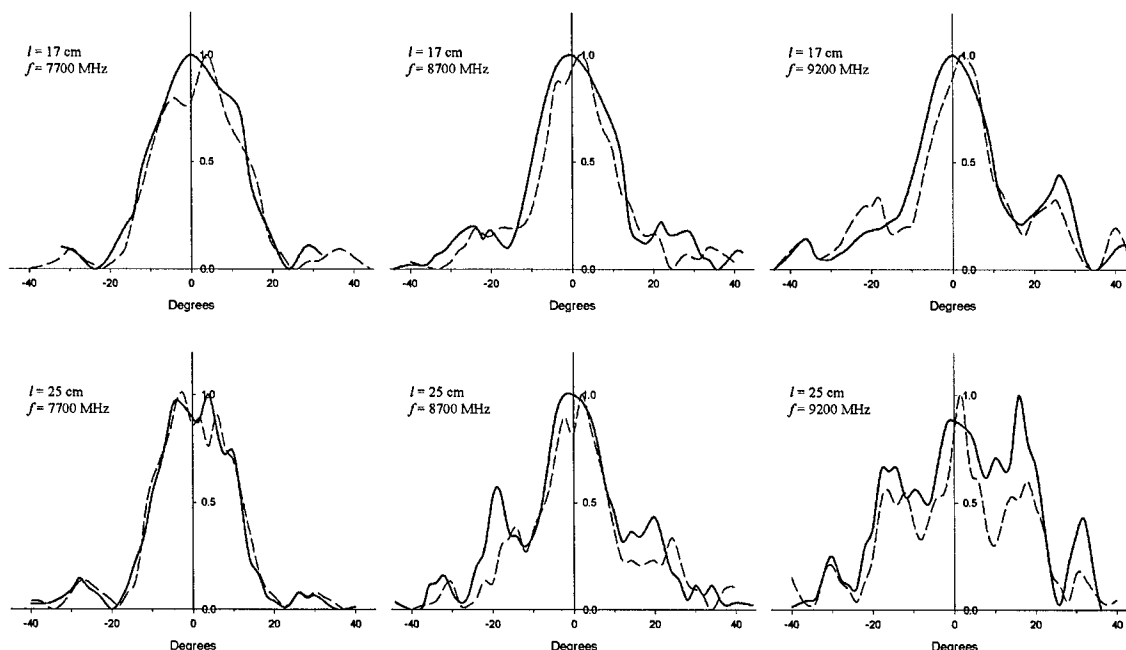


Fig.53. Power delivered to the receiving antenna (a.u.) vs. angle between the fixed rod antenna and direction to receiving antenna moving in the H-plane (solid curves) and E-plane (dashed curves) at different frequencies for two different antenna lengths (measured in the free space).

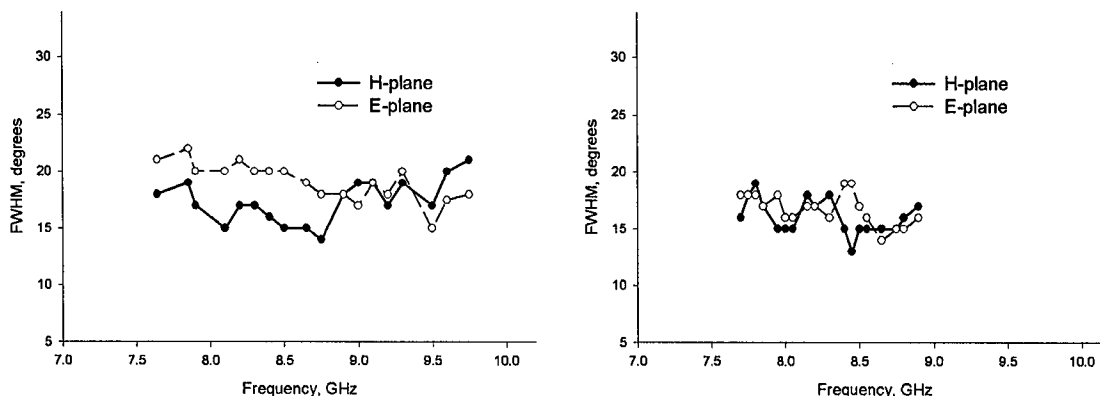


Fig.54. Radiation pattern angular width vs. frequency.  $l = 17$  cm (left plot) and 25 cm (right plot).

With regard to the measurements of the amplitude of reflected signal in the microwave transmission system incorporated into the LIA, our experiments have shown that the designed system can be matched within the required range of operating frequencies. A certain adjustment in the section matching the 23 mm diameter waveguide cross-section to 16 mm diameter dielectric-filled waveguide is needed to maintain matching at a fixed level as the frequency changes. It is achieved by little ( $\leq 1$  cm) displacement of the polyethylene rod as whole along the system axis. To obtain more frequency-independent characteristic of the system, special synthesis of axial profile of the rod input part is required. In any case, the fact that the reflected signal can be eliminated under conditions of real surrounding of the dielectric rod is important in the light of future experiments on gain demonstration in the antenna-amplifier with a powerful, pulsed microwave drive source.

### III. CONCLUSIONS

The concept of hybrid antenna-amplifier, a combination of a surface wave antenna with a relativistic Cherenkov amplifier for a controllable compact high-power microwave source has been explored through theoretical investigations, numerical simulations, and model experiments. The investigated configuration is based on the dielectric rod antenna fed through the waveguide serving simultaneously as the cathode holder in the linear induction accelerator, generator of high-current relativistic annular electron beam.

The one-dimensional nonlinear theory has been developed allowing one to perform simulations of the device with non-axisymmetric RF drive signal (operating  $HE_{11}$  mode of the dielectric rod) and accounting for higher-order modes involved into the process of interaction with the electron beam at harmonics of the drive frequency. The multimode simulations carried out have made possible to determine two characteristic sets of parameters appropriate for future detailed investigations of the antenna-amplifier. The difference between the two sets is in the physics of interaction at the nonlinear stage when the  $HE_{11}$  mode either dominates, or does not dominate, so that one may have in the output signal spectrum either combination of the main and harmonic frequencies with comparable power level, or typical for conventional Cherenkov amplifiers prevalence of the main frequency. The latter, less complicated case have been chosen for the initial future proof-of-principle experiments on gain demonstration in the antenna-amplifier. The 1-D simulations have shown that in this case, the output power transmitted in the  $HE_{11}$  mode at the main X-band frequency is at least 20 dB higher than the 2nd harmonic power in the higher-order  $TM_{01}$  and  $HE_{21}$  modes. The case of effective multiplication of the drive signal frequency is promising since novel schemes of tuning can be realized providing electronic control of the ratio of harmonic amplitudes in the radiation spectrum. It has been found that the harmonic content of the output signal can be controlled by changing the place of the beam removal out of the interaction space, or by variation of the input signal frequency, or by changing the input signal field polarization from linear to circular.

The two characteristic sets of parameters have been studied in full-scale numerical particle-in-cell simulations of the antenna-amplifier using the 3-D version of the code MAGIC. For the set providing the dominance of the operating  $HE_{11}$  mode and chosen for initial experiments to be done in the future to prove the concept, the achievable gain, bandwidth, and device efficiency have been found. At the peak gain frequency of  $\sim 9.3$  GHz, it reaches  $\sim 17$  dB with the interaction space length of  $\sim 25$  cm. The amplification band coincides with the frequency range of the available magnetron to be employed for microwave drive pulse production, and the efficiency reaches  $\sim 10\%$  at  $\sim 20$  MW output power. With the values of tangential electric field component at the rod surface corresponding to this power level, the surface breakdown can be eliminated, so that the obtained results allow for planning future experiments on the gain demonstration. For another set of parameters, the effect of drive signal frequency multiplication has been verified, and the possibility to control harmonics content in the output signal spectrum has been confirmed. Also, it has been shown that accounting for real conditions in the electron diode by means of explosive emission model results in lower gain and efficiency as well as in lower level of generated frequency harmonics.

The linear theory of Cherenkov interaction has been built for the case of annular electron beam in the waveguide with an inner disc-loaded conducting rod in order to compare achievable values of gain and bandwidth to the case of an inner dielectric rod. The dispersion relation of the system has been derived in the one-wave approximation valid for description of the instability in the fundamental quasi-TEM mode; its complex solutions have been investigated at different beam and structure parameters. The particular result of the

comparison is that the achievable gain in the quasi-TEM mode of the structure with the disc-loaded rod is much higher than that in the  $HE_{11}$  mode of the structure with the dielectric rod due to stronger beam-wave coupling at given beam-rod distances. At the X-band operating frequencies, the gain per unit length reaches  $\sim 3$  dB/cm. In addition, the  $-3$  dB bandwidth for the disc-loaded rod can be about twice wider under certain parameters due to weaker dispersion of the quasi-TEM mode. Nevertheless, advantages of dielectric rod, such as much easier input of the microwave drive signal and very good frequency separation of operating  $HE_{11}$  mode from others, make it more preferable for the antenna-amplifier device to be based on, if there were no problems connected with the near-surface plasma formation.

The latter issue has been studied in the model experiments on annular electron beam generation and transport in the guiding magnetic field with a dielectric rod inside in the absence of external microwave signal. The experiments have been conducted on the compact linear induction accelerator module specially modified to make it appropriate for the antenna-amplifier device. The parameters of electron beam and drift tube geometry corresponded to those chosen for the future proof-of-principle experiments and investigated in MAGIC simulations (except the dielectric rod material, for which plexiglas, polyethylene, and quartz were tested). In these studies, it has been shown that a dense plasma production from inside the cathode can be eliminated by means of "hiding" the triple point circle where the rod contacts the cathode inner surface deeply enough, far from the cathode edge. It has been found, however, that plasma is formed at the rod surface at the location of tapered buffer section between the drift tube and anode of the coaxial diode. The density of this near-surface plasma has been estimated by means of measuring the current delivered to the inner collector of the special composite Faraday cup and considering it as the electron saturation current. For a plasma of a few eV temperature, the density turns out to be  $\sim 10^{12}$  cm $^{-3}$  for all tested materials that is not so high to significantly affect the electrodynamic properties of the interaction space in an X-band device. Also, it has been found that in a great amount of shots, the UV radiation from the explosive emission cathode plasma heats the plastic rods near the cathode edge up to softening and some material transfer off, so that they are rather not appropriate for an operating device, and materials with high softening (melting) temperature like quartz or titanium silicate glasses should be employed in the antenna-amplifier.

The microwave transmission system to be incorporated into the LIA module, so that a circular antenna feed waveguide could serve as LIA cathode holder has been designed, fabricated, and tested. Studies of microwave transmission and antenna pattern without electron beam generation have been carried out using the low-power cw X-band oscillator tunable over 7.6-9.8 GHz frequency range. It has been shown that the real geometry of the device practically does not change the angular distribution of radiated power and its dependence on frequency in comparison with those of the isolated antenna. Measurements have shown expected directivities of tested antennas ( $\sim 15$ - $20^\circ$  FWHM width) and the growth of the side lobes level with increasing frequency. Also, it has been demonstrated that the reflected signal can be eliminated under conditions of real surrounding of the dielectric rod. This is important in the light of future experiments on gain demonstration in the antenna-amplifier with a powerful, pulsed microwave drive source.

Finally, the research performed allows us to consider the antenna-amplifier concept realizable. The initial design of the antenna-amplifier that is based on a dielectric rod antenna and driven by the electron beam ( $\sim 200$  keV, 1 kA) produced in the compact linear induction accelerator module has been elaborated, and most of the hardware required for the future experiments to prove the concept has been fabricated. It is assumed that an X-band microwave pulse compressor will be employed as an RF drive source. Now, we plan on the demonstration of gain in the device at the output radiation power level of 10-20 MW for pulses of up to tens nanoseconds duration.

#### IV. References

1. J. Benford and J. Swegle, High Power Microwaves, Artech House, Boston, 1992.
2. R. J. Barker and E. Schamiloglu, Eds., High Power Microwave Sources and Technologies, IEEE Press, Piscataway, NJ, 2001.
3. W. M. Manheimer, G. Mesyats, and M. Petelin, Applications of high-power microwave sources to enhanced radar systems, Chapter 5 of Applications of High-Power Microwaves, Artech House, 1994.
4. P. Wang, J. D. Ivers, J. A. Nation, S. Banna, and L. Schachter, A comparative study of high power, multistage TWT amplifiers, Proc. PAC'99, Particle Accelerator Conference, New York, 1999, p. 3600-3602.
5. G. V. Mel'nikov, A. V. Petrov, and A. S. Shlapakovski, Wall plasma in a wideband dielectric Cherenkov maser, Plasma Physics Reports, 2000, v. 26, no. 12, p. 1015-1026.
6. M. V. Kuzelev, O. T. Loza, A. A. Rukhadze, P. S. Strelkov, and A. G. Shkvarunets, Plasma relativistic microwave electronics, Plasma Physics Reports, 2001, v. 27, no. 8, p. 669-691.
7. Carlton H. Walter, Traveling Wave Antennas, McGraw-Hill, New York, 1965.
8. A. Shlapakovski, Relativistic TWT with a rod slow-wave supporting structure and a concept of hybrid antenna-amplifier device, In "Intense Microwave Pulses VI", Proc. SPIE - Int. Soc. For Optical Eng., Ed., Howard E. Brandt, Volume 3702, p. 108-113, 1999.
9. A. S. Shlapakovski, E. Schamiloglu, and I. I. Grushin, Multiplication of the drive signal frequency in a relativistic microwave amplifier with a rod slow-wave structure, Technical Physics, 2002, v. 47, no. 11, p. 1434-1439.
10. A. Shlapakovski, W. Jiang, and E. Schamiloglu, Numerical simulations of an antenna-amplifier – Cherenkov maser with a rod slow-wave structure operating in a non-axisymmetric mode, Proc. 14th IEEE International Pulsed Power Conference PPC-2003, Dallas, TX, 2003, p. 1169-1172.
11. N. J. Dionne, Harmonic generation in octave bandwidth traveling-wave tubes, IEEE Trans. Electron. Devices, 1970, v. 17, p. 365-372.
12. L. A. Vainshtein and V. A. Solntsev, Lectures on Microwave Electronics, Sov. Radio, Moscow, 1973 (*in Russian*).
13. Yu. A. Ilarionov, S. B. Rayevsky, and V. Ya. Smorgonsky, Calculations of Corrugated and Partially Filled Waveguides, Sov. Radio, Moscow, 1980 (*in Russian*).
14. J. A. Nation, On the coupling of a high-current relativistic electron beam to a slow wave structure, Appl. Phys. Lett., 1970, v. 17, no. 11, p. 491-494.
15. I. I. Vintzenko and E. G. Furman, Linear induction accelerators, Izvestiya VUZov, Fizika, 1998, no. 4, Suppl., p. 111-119 (*in Russian*).
16. S. N. Artemenko, V. A. Avgustinovich, P. Yu. Chumerin, and Yu. G. Yushkov, Energy extraction from an oversized cavity through a package of interference switches with summation of the output signals, Technical Physics, 2000, v. 45, no. 11, p. 1475-1477.
17. A. L. Fel'dshtein, L. R. Yavich, and V. P. Smirnov, Handbook on Elements of Waveguide Technique, Gosenergoizdat, Moscow-Leningrad, 1963 (*in Russian*).

## V. Presentation of Results

### *List of published papers and reports*

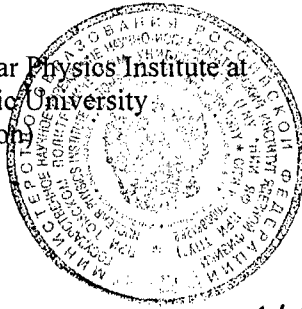
1. A. S. Shlapakovski, I. I. Vintizenko, A. V. Petrov, and E. Schamiloglu, "Hybrid Antenna-Amplifier: a Concept of High-Power Microwave Source and First Results of its Exploration," Proceedings of 15<sup>th</sup> International Conference on High-Power Particle Beams, BEAMS'2004, Saint Petersburg, Russia, July 18-23, 2004 – *to be published*.
2. A. S. Shlapakovski, "Cherenkov Interaction of a Hollow Relativistic Electron Beam with RF Fields of a Disc-Loaded Rod Antenna in a Circular Waveguide," Proceedings of 15<sup>th</sup> International Conference on High-Power Particle Beams, BEAMS'2004, Saint Petersburg, Russia, July 18-23, 2004 – *to be published*.
3. A. S. Shlapakovski, I. I. Vintizenko, A. V. Petrov, and E. Schamiloglu, "Hybrid Antenna-Amplifier: a Concept of High-Power Microwave Source and First Results of its Exploration," Proceedings of 13<sup>th</sup> International Symposium on High Current Electronics, Tomsk, Russia, 25-29 July, 2004, pp. 224-227.
4. A. S. Shlapakovski, "Cherenkov Interaction of a Hollow Relativistic Electron Beam with RF Fields of a Disc-Loaded Rod Antenna in a Circular Waveguide," Proceedings of 13<sup>th</sup> International Symposium on High Current Electronics, Tomsk, Russia, 25-29 July, 2004, pp.281-283.
5. A. S. Shlapakovski, I. I. Vintizenko, A. V. Petrov, and E. Schamiloglu, "Hybrid Antenna-Amplifier: a Concept of High-Power Microwave Source and First Results of its Exploration," 15<sup>th</sup> International Conference on High-Power Particle Beams, BEAMS'2004, ABSTRACTS, Saint Petersburg, Russia, July 18-23, 2004, p. 132
6. A. S. Shlapakovski, "Cherenkov Interaction of a Hollow Relativistic Electron Beam with RF Fields of a Disc-Loaded Rod Antenna in a Circular Waveguide," 15<sup>th</sup> International Conference on High-Power Particle Beams, BEAMS'2004, ABSTRACTS, Saint Petersburg, Russia, July 18-23, 2004, p. 147.

### *List of presentations at conferences and meetings*

1. A. S. Shlapakovski, I. I. Vintizenko, A. V. Petrov, and E. Schamiloglu, "Hybrid Antenna-Amplifier: a Concept of High-Power Microwave Source and First Results of its Exploration," 15<sup>th</sup> International Conference on High-Power Particle Beams, BEAMS'2004, Saint Petersburg, Russia, July 18-23, 2004 – *oral talk*.
2. A. S. Shlapakovski, "Cherenkov Interaction of a Hollow Relativistic Electron Beam with RF Fields of a Disc-Loaded Rod Antenna in a Circular Waveguide," 15<sup>th</sup> International Conference on High-Power Particle Beams, BEAMS'2004, Saint Petersburg, Russia, July 18-23, 2004 – *poster presentation*.
3. A. S. Shlapakovski, I. I. Vintizenko, A. V. Petrov, and E. Schamiloglu, "Hybrid Antenna-Amplifier: a Concept of High-Power Microwave Source and First Results of its Exploration," 13<sup>th</sup> International Symposium on High Current Electronics, Tomsk, Russia, 25-29 July, 2004 – *oral talk*.
4. A. S. Shlapakovski, "Cherenkov Interaction of a Hollow Relativistic Electron Beam with RF Fields of a Disc-Loaded Rod Antenna in a Circular Waveguide," Proceedings of 13<sup>th</sup> International Symposium on High Current Electronics, Tomsk, Russia, 25-29 July, 2004 – *poster presentation*.

SIGNATURES

Director of Nuclear Physics Institute at  
Tomsk Polytechnic University  
(Leading Institution)



Alexander I. Ryabchikov

Project Manager

Anatoli S. Shlapakovski